UNIVERSIDADE FEDERAL DE SANTA CATARINA
CAMPUS JONIVILLE
CURSO DE ENGENHARIA NAVAL

RODRIGO MICHELS

NUMERICAL SIMULATION OF FLEXURAL TESTS IN METAL CERAMIC COMPOSITES

Joinville, 2015

RODRIGO MICHELS

NUMERICAL SIMULATION OF FLEXURAL TESTS IN METAL CERAMIC COMPOSITES

Trabalho de Conclusão de Curso apresentado como requisito parcial para obtenção do título de bacharel em Engenharia Naval, no curso de Engenharia Naval da Universidade Federal de Santa Catarina.

Orientador: Hazim Ali Al-Qureshi, PhD
Universidade Federal de Santa Catarina

Co-orientador: Rolf Janβen, Dr.-Ing.
Universidade Técnica Hamburg-Harburg

Joinville, 2015

RODRIGO MICHELS

NUMERICAL SIMULATION OF FLEXURAL TESTS IN METAL CERAMIC COMPOSITES

Esse Trabalho de Graduação foi julgado adequado para a obtenção do título de bacharel em Engenheria Naval, e aprovado em sua forma final pela Comissão examinadora e pelo Curso de Graduação em Engenharia Naval da Universidade Federal de Santa Catarina.

Joinville, 07 de julho de 2015

Prof. Thiago Pontin Tancredi, Dr. Eng.
Coordenador do Curso

COMISSÃO EXAMINADORA

Prof. Hazim Ali Al-Qureshi, PhD
Presidente da banca - Orientador

Prof. Gabriel Benedet Dutra, PhD
Membro da banca

Prof. Alexandre Mikowski, Dr.
Membro da banca

Dedico este trabalho à toda minha família, em especial meus pais, por terem me incentivado durante todo o percurso de minha formação.

AGRADECIMENTOS

Agradeço a todos que de alguma forma contribuíram no decorrer desta jornada, em especial:

A Deus, por me agraciar com a vida, a saúde e a beleza deste mundo.

A toda minha família, em especial meus pais, por terem cultivado em mim seu amor e seus ensinamentos, cujos princípios foram essenciais em todas as minhas conquistas.

Aos meus amigos e colegas, pelo companherismo dedicado em todos momentos, pelas histórias inesquecíveis, por serem uma segunda família para mim. Em especial, aos meus amigos do Sedentários F.C. e do CONEMB, os quais nunca esquecerei.

Aos diretores, sevidores e professores do Campus Joinville, em especial meu orientador, Prof. Hazim, por ser meu incentivador, por instigar a busca pelo conhecimento e por ter proporcionado a oportunidade de realizar meu sonho de fazer intercâmbio. Agradeço também à estimada Amarilis Laurenti, pela amizade e pelos ensinamentos, tão importantes quanto qualquer disciplina que cursei.

Aos colegas e amigos do Instituto de Cerâmicas Avançadas da Universidade Técnica de Hamburg-Harburg, em especial ao Dr.-Ing. Janβen e ao Msc. Robert Besler, por terem me auxiliado no desenvolvimento deste trabalho.

A todos que participaram desta trajetória, meu muito obrigado.

.

RESUMO

O presente trabalho tem como objetivo simular com um software o processo de produção (compactação e sinterização) e ensaios de flexão em materiais compósitos de metal e cerâmica. Tais compósitos são compostos de particulados e/ou grãos dentro de uma matriz. Esses materiais particulados são simulados utilizando o Método de Elementos Discretos (MED), que calcula o movimento de um número finito de partículas de um sistema ou durante um processo. Com o programa de MED é possível realizar a produção de vigas em microescala pela compactação de partículas de alumina e aço, com três variações de composição. Um modelo de ligação é utilizado para simular o material após a sinterização e posteriormente essas vigas são submetidas a um teste de flexão de três pontos, onde é possível obter o módulo de elasticidade do material compósito. Resultados satisfatórios foram obtidos ao comparar com dados de experimentos reais. O modelo de ligação foi validado para o material a partir da análise da microestrutura simulada e dos resultados do módulo de elasticidade.

Palavras-chave: *Compósitos de metal e cerâmica, Métodos de Elementos Discretos, Compactação e sinterização, Ensaios de flexão.*

ABSTRACT

The objective of the the present work is to simulate with a software the production process (compaction and sintering) and flexural tests in a metal ceramic composite. This composite is composed of particles or flakes inside a matrix. This kind of particulate materials are simulated with the Discret Element Method (DEM), which calculates the movement of a finite number of particles in a sistem or during a process. With the DEM software, it is possible to carry out the production of beams in a microscale by the compaction of steel and alumina particles, with three variations of composition. A bonding model is used to simulate the material after the sintering process. Afterwards, three point bending test are carried out in the beams and the elastic modulus of the material is obtained. Satisfatory results were obtained by comparing with real experimental data. The bonding model was validated for the material by the analisys of the simulated microstructure and the results on the elastic modulus.

Keywords: *Metal and ceramic composites, Discret Element Method, Compaction and sintering, Flexural tests.*

LIST OF FIGURES

LIST OF TABLES

LIST OF ABBREVIATIONS

DEM	Discrete Element Method
P/M	Powder Metallurgy
CIP	Cold Isostatic Pressing
CFD	Computational Fluid Dynamics

LIST OF SYMBOLS

Latin letters

L	distance between lower cylinders	m
a	distance between lower and upper cylinders	m
F	force on cylinders	N
h	height of the beam	m
w	width of the beam	m
E	elastic modulus	Pa
I	moment of inertia	m^4
Δz	displacement of upper loads	m
m	mass	kg
$\mathbf{r}$	particle position	m
$\mathbf{v}$	particle velocity	$m \cdot s^{-1}$
$\mathbf{F}$	force acting on particle	N
$\mathbf{F}_c$	contact force on particle	N
$\mathbf{F}_{pp}$	adhesion force on particle	N
V	particle volume	m^3
p	pressure	Pa
$\mathbf{u}_g$	gas velocity	$m \cdot s^{-1}$
g	gravity	$m \cdot s^{-2}$
$\mathbf{T}$	torque acting on particles	N·m
t	time	s
R	particle radius	m
$\mathbf{n}_{ij}$	normal unit vector	-
$\mathbf{t}_{ij}$	tangential unit vector	-
$\mathbf{v}_{ij}$	relative velocitiy of contact particles	$m \cdot s^{-1}$
k_n	normal contact stiffness coefficient	$N \cdot m^{-1.5}$
E^*	equivalent elastic modulus	Pa
R^*	median radius of contact particles	m
m^*	effective mass of contact particles	kg
e	coefficient of restitution	-
W_{kin}	kinetic energy	J
G^*	equivalent shear modulus	Pa
$\bar{F}_b$	force acting on the bond	N
$\bar{M}_b$	moment acting on the bond	N·m
A	area	m^2
J	polar moment of inertia	m^4
$\bar{k}_n$	normal stiffness per unit area	$N \cdot m^3$
$\bar{k}_t$	tangential stiffness per unit area	$N \cdot m^3$

r_b	bond radius	m
L_b	bond lenght	m
$\bar{\sigma}$	tensile strength	Pa
$\bar{\tau}$	shear strength	Pa
R^c	contact radius	m
N	number of particles	-
X	fraction of the number of particles	-
L_{beam}	length of the beam	m
CN	average coordination number	-
v_{load}	loading speed	$m \cdot s^{-1}$
T_r	rayleigh time step	s
d	particle diameter	m

Greek letters

ε	porosity	-
β	interphase momentun transfer coefficient	$kg \cdot m^{-3} \cdot s^{-1}$
ω	particle angular velocity	$rad \cdot s^{-1}$
δ_n	normal contact overlap	m
η	damping coefficient	$N \cdot s \cdot m^{-1}$
ν	poisson ratio	-
μ	friction coefficient	-
δ_t	tangential displacement	m
$\Delta\delta$	overlap increment	m
$\Delta\theta$	rotational angles	rad
ρ	density	$kg \cdot m^3$
ρ_p	packing density	-
ρ_r	relative density	-
φ	volume fraction	-

Indexes

i	identity of the element
j	identity of the element
n	normal direction
t	tangential direction
c	contact
pp	particle-particle
b	bond
st	steel
al	alumina
tot	total

SUMMARY

1. INTRODUCTION

The development of advanced composite materials is relatively recent. Due to their unique characteristics, these composites are used in various vehicular systems, including in ships. Combining different metals, ceramics or polimers it is possible to produce composites for the required application. Particularly, metal and ceramic composites are used to fabricate thermocouple protection tubes, mechanical seals, gas-turbine flame-holders and engine cylinder liners (RICHERSON, 2006).

One possible combination of metal and ceramic used to fabricate composites is constituted by steel and alumina. This composite is produced by techniques of powder metallurgy (P/M). The final product is composed of interpenetrating aggregates or particles in a matrix, which can be either metal or ceramic. Final properties and microstructure depend on the amount of each material and porosity level present in the product. The final product can be manufactured with the necessary requisites. This characteristic makes these types of materials very attractive for the industry.

In the past decade, the utilization of computer simulations to evaluate properties and behaviors of particulate materials increased. They are a interesting alternative for the analysis of real physical problems compared to physical experiments, which are time and money spending. Depending on the type and procedure of the simulations, they can be much faster and easier to be executed.

To simulate particulate composites the discrete element method (DEM) is widely used. With this mathematical model it is possible to simulate each particle in a micro scale and to achieve a good outlook on the motion and forces acting between them. DEM softwares also provide various contact models between particles, enabling the simulation of different processes. The bonding model used in the present work is one of the avaible models in the software. The composite subjected to this model is considered as an approach of the sintered material. In literature, no

studys were found using this bonding model as presented in this work. Therefore, by validating this model, new possiblities are created for the utilization of DEM and its tools for the analysis of composite materials.

1.1. Objectives

1.1.1. General objective

The objective of the present work is to discuss the aplicability of the basic contact model and the bonding model between particles of the DEM by using simulation of flexural tests on metal ceramic composites and comparing with real experiments.

1.1.2. Specific objectives

- Study the characteristics of the DEM and the mathematical models in order to develop the methodology to be applied in the simulations;
- Generate beams with three different compositions of steel and ceramic mixture using the basic contact model and the bonding model of the DEM software;
- Analyze and compare the microstructure and particle distribution within the beams in the simulation and in real samples;
- Carry out the flexural tests in order to analyze the flexural behavior and to evaluate the elastic modulus of the simulated material;
- Compare and discuss the simulation methodology and results with real experiments in order to validate the DEM models between particles used.

2. THEORY

The present chapter presents the fundamental theory needed for the clear understanding of the work. The chapter is divided in three parts. First, the fundamentals of powder processing will be explained. It is presented the main steps on the production, which are powder preparation, shape-forming and sintering. Furthermore, it is presented the properties and applications for the composites produced by this technique.

The second section explains the experimental test called flexural test or bending test, which is used to calculate mechanical properties (e.g. the elastic modulus) of a material. the algebraic equations for the calculation of such properties will be presented.

The third section of this chapter treats about the DEM, which is the mathematical model used for the simulations. The numerical description of the method, the basic contact model used to calculate the motion of particles during a collision and the bonding model used as an approach for the sintered material are presented.

2.1. Powder Processing

Powder processing is a industrial technique for the manufacture of products by using particles as a raw material. The most common materials used in this technique are metals, which process is specially called powder metallurgy (P/M), and ceramics. The properties and applications for these material and also for composites produced by the mixture of both are shown in the first subsection.

The steel and alumina composite studied in the present work is produced by powder processing. Subsections two to four explain the principles involved in this technique. It generally consists of three basic steps: (1) powder preparation, (2) shape-forming and (3) densification. The first one consists in the processes of particle sizing, addition of lubricants or binders, blending and drying. The second includes compaction, casting or plastic forming. The last step, also called sintering, consists of three main stages, which will be briefly explained, leading to the densification of the particulate material.

2.1.1. METAL, CERAMICS AND COMPOSITES: PROPERTIES AND APPLICATIONS

Metal and ceramics play important roles in all kinds of engineering applications. Their outstanding properties provide a wide variety of possible applications, even more when these materials can be combined in one unique product by the powder metallurgical processing route.

In general, ceramics are hard, brittle, with low electrical and thermal conductivity, low thermal expansion, good chemical and thermal stability, good creep resistance, high elastic modulus, and high compressive strengths that are retained at elevated temperature. In the past 100 years a family of “advanced ceramics” emerged. These materials now provide enhanced functional properties that make them attractive for many applications. The base materials currently include silicon nitride, silicon carbide, zirconia, alumina, sialons, boron carbide, boron nitride, titanium diboride, and ceramic composites. Applications include a wide variety of wear-resistant parts (including bearings, seals, valves, and dies), cutting tools, punches, dies, and engine components, as well as use in heat exchangers, gas turbines, and furnaces (Figure 1a) (BLACK; KOSHER; 2008). It is also possible to find studies for application of advanced ceramics in the naval area. Miyagi (1993), for example, tested the differences in heating and emissions of a marine engine by covering the combustion chamber wall with different kinds of ceramics materials.

Meanwhile, the common metals are iron, copper, aluminum, magnesium, nickel, titanium, lead, tin, and zinc as well as the alloys of these metals, such as steel, brass, and bronze. They possess the metallic properties of high thermal and electrical conductivity, they are relatively ductile and some have good magnetic properties. Especially with the powder metallurgy is possible to produce small, intricate parts of high precision, often eliminating the need for additional machining or finishing. There is little material waste and controlled degrees of porosity or permeability can be produced. Some examples of applications include friction materials, structural parts (e.g. engine, transmissions, turbines, pumps, valves and hardware parts), cutting tools, magnetic materials, electronic components, etc. (Figure 1b). (EUROPEAN POWDER METALLURGY ASSOCIATION, 2008)

Figure 1 - (a) examples of advanced ceramic applications and (b) examples of powder metallurgy products.

(a) (b)

Source: Black and Kohser (2008).

In the past decades there was an increasing on the development and fabrication of composite materials. They combine two or more materials into a single product to achieve specific properties, which could not be achieved with the individual components by themselves. For example, ceramics do not degrade at high temperature but lack ductility. The combination of ceramic particles in a metal matrix results in a composite that presents better ductility than the ceramics alone along with good high-temperature resistance. Particularly, the oxide-based cermets (e.g. Al_2O_3-Cr, MgO-Cr) show an outstanding characteristic: the metal or ceramic can be either the particle or the matrix constituent. Thus, a wide range of property is available and the composition can be tailored to specific requirements. They are extensively used in high-speed cutting tools, and also as flow control pins,

thermocouple protection tubes, mechanical seals and gas-turbine flame-holders. (SCHWARTZ, 2008)

Although the possible material combinations in composites are virtually unlimited, the constituent forms are more restricted. They can be: fibers, particles, lamina or layers, flakes, fillers, and matrixes (Figure 2) (SCHWARTZ, 2008). The present work focus only on a composite which can be constituted of particulates or flakes, which are called inclusions, inside a matrix, and are produced by means of the powder metallurgy. Both metal and ceramic can be the matrix or the inclusions, and the microstructure characteristic depends on the amount of each material present in the composite. Three situations can be found on such composite: isolated inclusions on the matrix, aggregates or percolation. The first occurs when the fraction of the inclusion present in the mixture is very low, and the sintered body presents a microstructure of a particulate composite. However, when the fraction of inclusions increases, the particulates connect and form the aggregate situation. With a higher fraction of the inclusion material, the aggregates can interconnect, and a percolating particle network – or "skeleton" – is formed. In the case of a composition with about 50 vol.% of both material, there is no visible difference between matrix and particulate, and both steel and alumina possess a continuous network of agregates. The fraction limits between the three situations depend strongly on the particle size ratio. This behavior can be observed with real experiments and a detailed discussion will be presented later.

Figure 2 - Basic structure of some classes of composites.

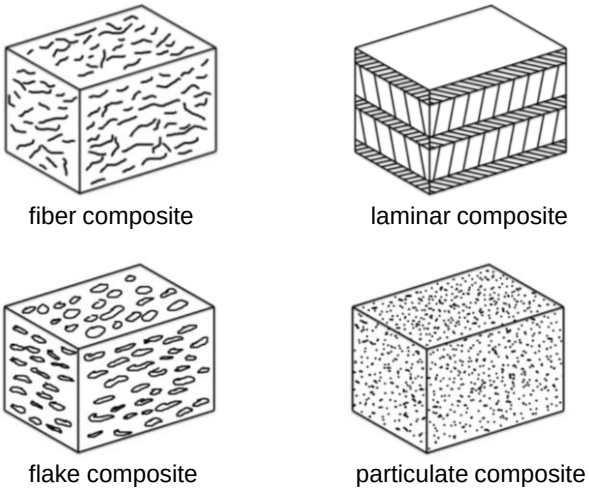

Source: Elaborated by the author.

2.1.2. POWDER PREPARATION

The first step in manufacturing products by using powders is the material preparation. The powder utilized must present high controlled characteristics, since they have a significant effect on the final properties of the product. To achieve the optimal powder some steps are required (Figure 3).

Figure 3 - Sub-processes in powder preparation.

Source: Elaborated by the autor.

First, the raw materials must be carefully selected. Metal powders are normally obtained by melt atomization, while advanced ceramics such as alumina are produced by chemical and thermal processes applied on natural minerals.

After the production and selection of the raw material, it is often necessary to eliminate aggregates and agglomerates. Many different powder synthesis and sizing techniques have been developed, some mechanical, chemical, or a combination of both. One example is the attrition milling, where the powder is placed in a closed cylindrical container with grinding media (balls, short cylinders, or rods), which are agitated by a series of stirring arms mounted to an axial shaft. The attrition mill can be used at the same time to grind, blend powders and add binders, making the process of powder preparation much faster.

To achieve a component without defects and with uniform properties, the addition of binders, lubricants or compaction aids is often required. For the composition of steel and alumina, for example, an addition of a very small amount of binder modifies significantly the behavior during compression, increasing the green strength. However, the binder is an impurity to the product and must be romeved before the sintering.

The slurry formed during the mixing usually needs to be dried and sieved before the shape-forming process. The drying process can be carried out by spray-

drying or using a simple rotatory evaporator. The sieving is carried out afterwards to break the bigger agglomerates into smaller ones that can be easy compressible.

2.1.3. SHAPE-FORMING

The shape-forming is the process of consolidation of the loose powder into the required shape, known as green body or compact, which must be sufficiently strong to withstand ejection from the die and subsequent handling before sintering. This is a critical operation in the fabrication, since the final shape and mechanical properties are essentially determined by the level of density and uniformity. (EUROPEAN POWDER METALLURGY ASSOCIATION, 2008)

There are many compaction techniques for ceramics and metals, most can be used to produce composites. They can be divided in slip casting, tape casting, plastic forming and pressing, as is presented in Table 1.

Table 1 - Major shape-forming techniques.

Slip Casting	**Tape Casting**	**Plastic Forming**	**Pressing**
Drain castings	Doctor blade	Extrusion	Uniaxial
Solid casting	Waterfall	Roll Forming	Cold Isostasy
Vacuum casting		Injection Molding	Hot pressing
Pressure casting		Compression molding	Hot isostatic
Centrifugal casting			
Fugitive-mold			
Gel casting			
Electrophoretic deposition			

Source: Richerson (2006).

The slip casting and tape casting are commonly used for traditional ceramics, since involve the suspension of particles in a liquid. The slip formed is then casted

into porous plaster molds. As presented in Table 1, there are a number of variations to this process, depending on the viscosity of the ceramic-liquid suspension.

Plastic forming involves producing shapes from a mixture of powder and additives that are deformable under pressure. Four types of compression method are used in plastic forming and are extensively used for traditional ceramics, since the compositions contain clay and are workable with water. The extrusion process is carried out forcing the mix trough a shape die by rotation of an auger. In the roll forming process, the mix is passed between two cylinders (rolls) that are rotating in opposite directions. In the compaction molding the mix is compressed between platens of a shaped die. The injection molding process is used not only with traditional ceramics, but also with composites such as polimers and metal and ceramics composites. In this process, the mix is preheated and forced through an orifice that leads to a mold, where it cools and hardens to the configuration of the cavity.

Pressing is widely used fabricate products of metal, ceramic and their composites. It is accomplished by placing the powder into a die and applying pressure to achieve compaction. The selection of additives is important: the green body must exhibit adequate strength for handling and inspection and the friction on particle contacts and particle-wall contacts must be low to avoid flaws. The commonly used methods are uniaxial and isostatic pressing, which can be carried out consecutively to accomplish higher green densities and a homogeneous density distribution. (RICHERSON, 2006)

The uniaxial pressing, involves the compaction of powder into a rigid die by applying pressure along a single axial direction through a rigid punch, plunger, or piston. Figure 4 presents the typical compaction sequence for a mechanical press. With the bottom punch in its fully raised position, a feed shoe moves into a position above the die to fill the powder inside the die. The bottom punch descends to a preset fill depth and the shoe retracts, with its edges leveling the powder. The upper punch then descends and compacts the powder as it penetrates the die. During the compaction, the granules are crushed and a mechanical redistribution of the particles takes effect. The upper punch then retracts and the bottom punch rises to eject the green compact. When the pressure is applied by only one punch, it is vey difficult to transmit uniform pressures and produce uniform density throughout a compact,

especially when the thickness is large. By using a double-action press, where pressing movements occur from both top and bottom, thicker products can be compacted to a more uniform density distribution. (BLACK; KOSHER, 2008)

Figure 4 - Typical compaction sequence. Loose powder is shaded; compacted powder is solid black.

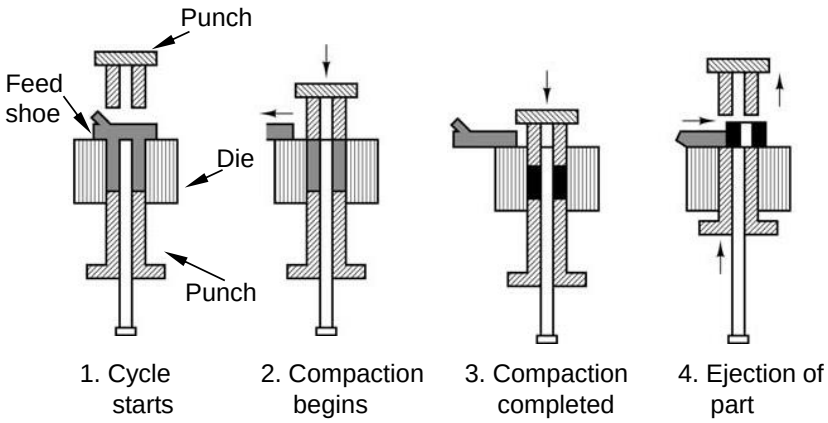

Source: Black and Kohser (2008).

Some limitations of uniaxial pressing can be overcome by applying pressure from all directions instead of only one or two directions. This is referred as cold isostatic pressing (CIP). There are many variations on using the CIP. Figure 5 illustrates the wet-bag process. Powder is weighed into a rubber bag and a metal mandrel is inserted, making a seal with the mouth of the rubber bag. The sealed bag is placed inside a high-pressure chamber filled with a fluid (normally a soluble oil/water mixture) and is hydrostatically pressed. Once the pressing is complete, the pressure is released slowly, the mold is removed from the chamber, and the green compact is removed from the mold. (BARRY; GRANT, 2007)

Figure 5 - Schematic of a wet-bag isostatic pressing.

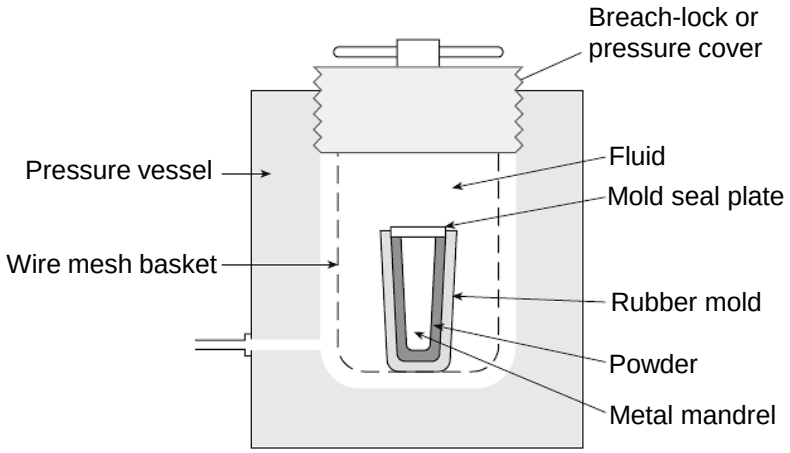

Source: Barry and Grant (2007).

2.1.4. SINTERING

In the sintering process step, the pressed-powder compacts, called green body, are heated in a controlled atmosphere to a temperature below the melting point but high enough to permit solid-state diffusion. This temperature is held for a sufficient time to permit removal of the pores between particles and strong bonding between adjacent particles. (RICHERSON, 2006)

Table 2 - Stages of sintering and corresponding processes.

1st Stage	**2nd Stage**	**3rd Stage**
Rearrangement	Neck growth	Much grain growth
Neck formation	Grain growth	Discontinuous pore phase
	High shrinkage	Grain boundary pores eliminated
	Pore phase continuous	

Source: Richerson (2006).

Theories about the microscopic dynamics during sintering have provided the subject matter of innumerable conferences and scientific papers. For composites of

two different materials such as ceramic and metals the contact interface between particles after sintering plays a big role on the mechanical properties.

A simplified approach of the sintering mechanisms in a unique material is listed in Table 2, with three main stages. The transitions during the stages are shown in Figure 6. The initial stage involves rearrangement of particles and initial neck formation at the contact point between each particle. The rearrangement consists of slight movement or rotation of adjacent particles to increase the number of contacts.

Figure 6 - Trasitions occurring on the microstructure during the three stages of sintering.

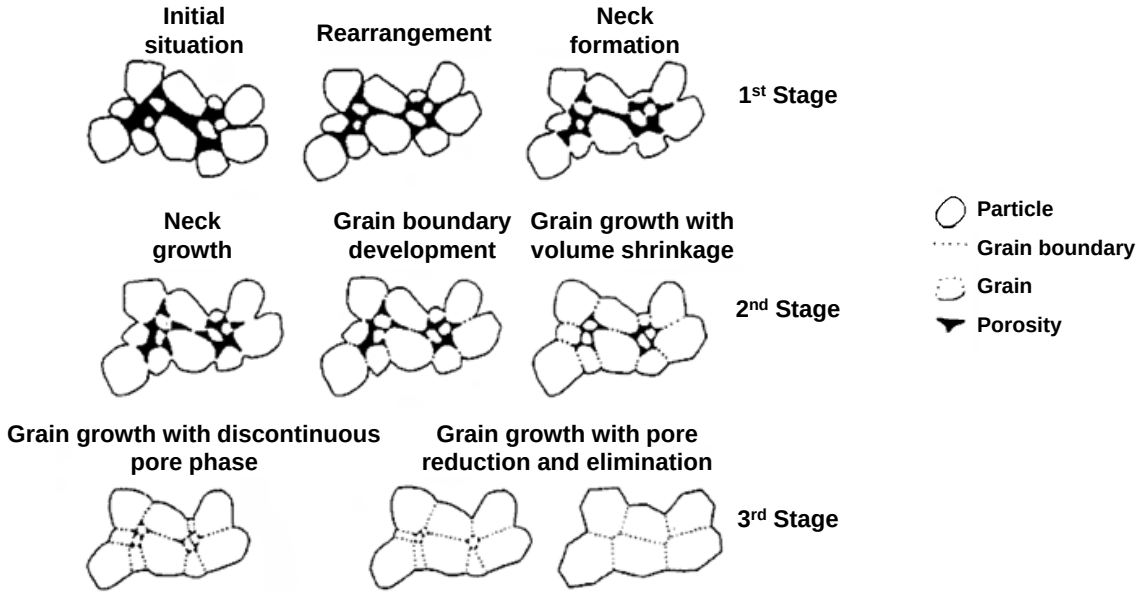

Source: Richerson (2006).

During the second stage the necks between particles grow and the porosity decreases, with the centers of the original particles moving close together. This results in shrinkage equivalent to the amount of porosity decrease. The grain boundaries start to move and one particle (now called grain) starts to grow while the adjacent grain is consumed. (RICHERSON, 2006)

The last stage involves the final removal of porosity by vacancy diffusion along grain boundaries. Therefore, the pores must remain close to the grain boundaries. Pore removal and vacancy diffusion are aided by movement of grain boundaries and controlled grain growth. However, if grain growth is too rapid, the grain boundaries can move faster that the pores and leave them isolated inside a grain. The final

distribution of grains and pores is referred to as microstructure (RICHERSON, 2006). During sintering of metals and composites, not all of the porosity is removed. Conventional pressed-and-sintered P/M products generally contain between 5 and 25% residual porosity. (BLACK; KOSHER, 2008)

2.2. Flexural Tests

The flexural test, also known as bending test, is an experimental method used to study the mechanical behavior (tension-compression) of a material under a specific applied load. It is a usual test for material development, quality control, characterization and data generation purposes.

The load applied on the material during this test causes a bending of the material specimen. Typically, it is possible to calculate the values for the elastic modulus of the material, which is the main objective of the present work, the strength of the specimen and in certain cases, the fracture toughness. The advantage of this test is the easy sample preparation and testing. However, the results can be sensitive to the sample, loading geometry and loading rate.

Several studies have used the bending tests to evaluate the mechanical properties of materials. Gogotsi (2003), for example, studied the fracture toughness with a three-point test in ceramics and ceramics composites based on alumina, zirconia and silicon nitride. Sharma and Gupta (2012) evaluated the flexural strength in a carbide reinforced (tungsten-based) metal–matrix composite cladding on austenitic stainless steel substrate.

The test is commonly carried out with a universal testing machine. The sample is usually a beam, which is disposed above two fixed bearing cylinders set a distance *L* from each other. The loading is carried out by lowering one cylinder at the center of the beam from above at a constant rate. The setup with one loading cylinder is called three-point test. The loading can also be carried out lowering two cylinders at a distance *a* from the lower support, which is called four-point test (Figure 7).

Figure 7 - Schematic of a four-point bening test.

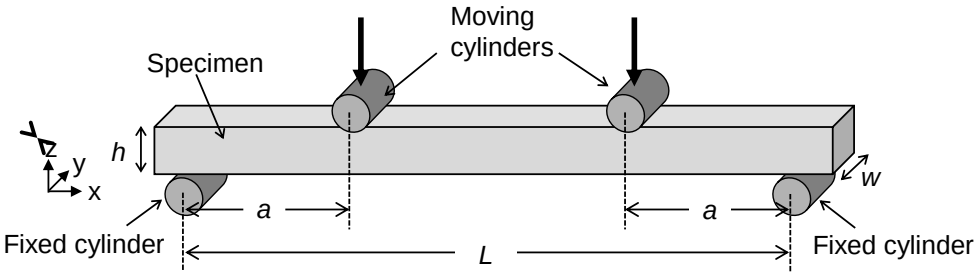

Source: Elaborated by the author.

The bearing cylinders used for supporting and loading must be carefully set, otherwise it could influence the tests. Figure 8 shows a typical fixture for a four-point bending test. The two support cylinders must be fixed, while the loading ones must not present vibrations or movement in any direction but downwards. However, they shall be free to rotate in order to relieve frictional constraints (with the exception of the middle-load bearing in three-point test which need not rotate). The fixture that maintains the cylinders in place must be hardened and allow some articulation or pivoting. This ensures the pairs of cylinders pivot together about an axis parallel to the specimen long axis, in order to match the specimen surfaces. (AMERICAN SOCIETY FOR TESTING AND MATERIALS, 2013)

The properties of the cylinders must no influence the tests. They must be constituted of a material harder than the specimen material to ensure that no elastic deformation occurs on the cylinders, which could influence the elastic response of the specimen during bending. The roughness of the cylinders must be low to decrease the friction coefficient with the beam.

Figure 8 - Four-point bending test fixture.

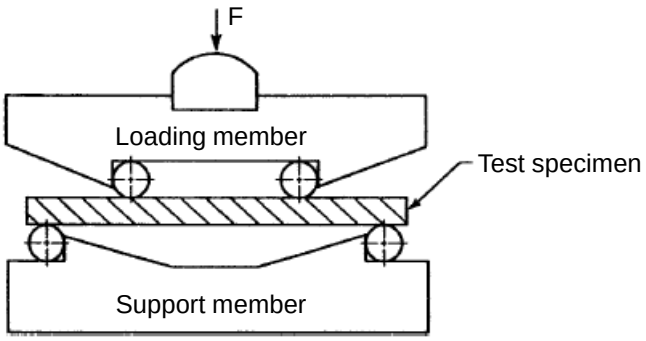

Source: American Society For Testing And Materials (2013).

The specimen to be tested must present some specifications. Grinding and final machining can be necessary, depending on the type of test required. A high surface roughness can damage the cylinders during the loading. The samples do not need to present perfect surface parallelism, since the fixtures of the test machine are articulated. However, to achieve better results it is important that the beam is plan parallel. The geometry of the beam must be measured before the loading for the calculation of the elastic modulus.

During the test the upper cylinders move downwards, usually at constant rate and the beam starts to deflect in a circular curve in response to the forces and moments acting. This deflection will create different zones of stresses in the interior of the beam (Figure 9). On the upper part, a compression region is formed while the lower part is in tension, and a neutral axis with state of free stress is found right in the middle of the beam. The higher the ductility of the material, i.e., the lower its elastic modulus, more the beam will bend.

Figure 9 - Moments and stresses acting on the beam during the loading.

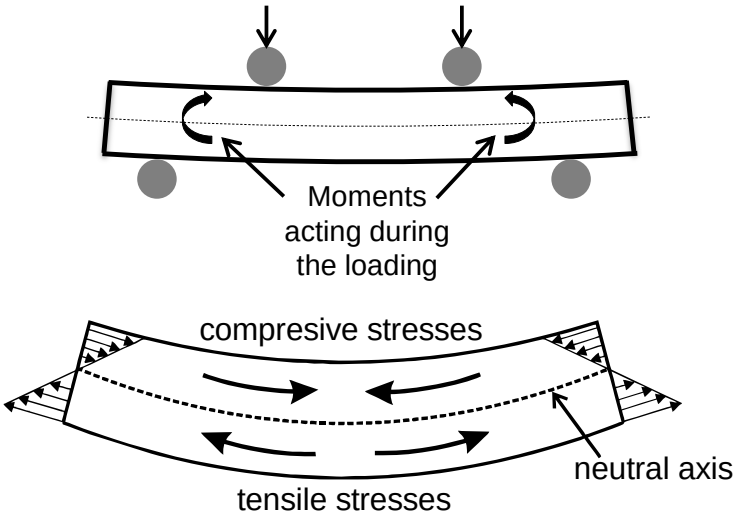

Source: Elaborated by the author.

The flexural stress is computed based on simple beam theory with the assumptions that the material is isotropic and homogeneous, the elastic modulus in tension and compression are identical and the material behaves linearly elastic. The modulus of elasticity in four-point bending, which is carried out in the present work, is calculated according to the Bernoulli-Euler beam theory.

Figure 10 presents the deflection of a beam under a pair of loads. The forces F_1 and F_2 represent the load of upper cylinders, placed at the same distance a from supports. When the loading is carried out, the longitudinal axis is deformed into a curve, called the deflection curve of the beam. The deflection Δz is the displacement in z direction of any point on the longitudinal axis. The deflection curve z is calculated as a function of distance x, as follows:

$$z = \begin{cases} \dfrac{\Delta F^{tot} x}{12 E I_y} \cdot \left(3La - 3a^2 - x^2\right) & (0 \le x \le a) \\ \dfrac{\Delta F^{tot} a}{12 E I_y} \cdot \left(3La - 3x^2 - a^2\right) & (a \le x \le L - a) \end{cases} \quad (1)$$

Where $\Delta F^{tot} = \Delta(F_1 + F_2)$ is the sum of forces on each upper load, E is the elastic modulus of the material and I_y the moment of inertia, which for a beam with width w and height h (Figure 7), is:

$$I_y = \frac{1}{12} w h^3 \quad (2)$$

Figure 10 - Deflection of a simple beam under a pair of loads.

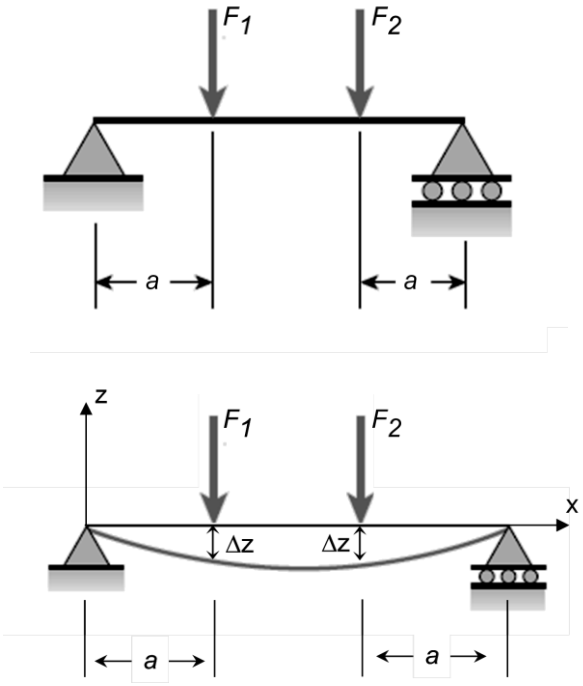

Source: Gere (2008).

The testing machine in which the bending is carried out measures the displacements of the cylinders (∆z in Figure 10) and the reaction forces on them, which are F_1 and F_2 in equation 1. With these values a force-displacement curve is plotted. Figure 11 presents a typical curve obtained with the test.

Figure 11 - Typical force-displacement curve for a bending test. The force increases almost linearly with the displacement.

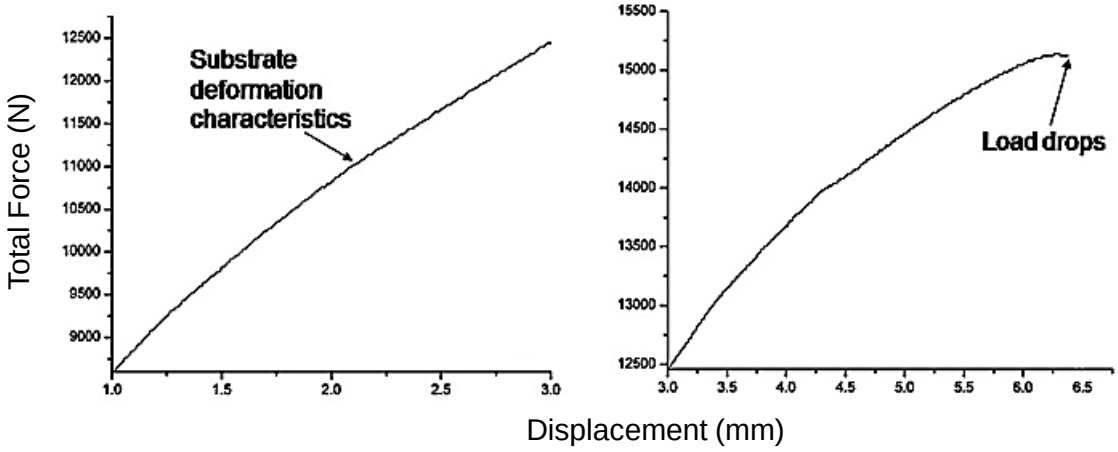

Source: Sharma and Gupta (2012).

The value ∆z, which is the displacement of the upper loads, is also the value for the deflection of the beam when x = *a* and x = *L* - *a*, where the upper cylinders are placed. Thus, by using equation 1 for x = *a* and x = *L* - *a*, the following expression is obtained:

$$z(\mathrm{x}=a)=\Delta \mathrm{z}=\frac{\Delta \mathrm{F}^{\mathrm{tot}} a}{12EI_{\mathrm{y}}}\left(3La-4a^2\right) \tag{3}$$

Simplifying equation 3 and resolving for the elastic modulus *E*:

$$E=\frac{La^2\Delta \mathrm{F}^{\mathrm{tot}}}{4I_y\Delta \mathrm{z}}\left(1-\frac{4a}{3L}\right) \tag{4}$$

The parameter *a* can be varied from 0.25*L* to 0.5*L*, where 0.25*L* is the most typically used 4-point bending setup and *a* = 0.5*L* is a 3-point bending test. The elastic modulus for the 3-point bending is calculated as:

$$E^{3\,point} = E^{4\,point}\left(a \to L/2\right) = \frac{L^3 \Delta F}{48 I_y \Delta z} \tag{5}$$

The three-point test configuration exposes only a very small portion of the specimen to the maximum stress. Therefore, three-point flexural strengths are likely to be much greater than four-point flexural strengths. Three-point flexure has some advantages. It uses simpler test fixtures, it is easier to adapt to high temperature and fracture toughness testing and it is sometimes helpful in Weibull statistical studies. However, four-point flexure is preferred and recommended for most characterization purposes. (AMERICAN SOCIETY FOR TESTING AND MATERIALS, 2013)

2.3. Discrete Element Method

The DEM is a numerical method used to simulate the motion of a finite number of individual elements (particles) in a system or during a process. It was developed by Cundall and Strack (1979) to solve problems of rock mechanics. Since then it is used in computational systems to simulate various kinds of processes, especially in powder technology, rock mechanics and particle flow. DEM has also been coupled with computational fluid dynamics (CFD) to describe particle–fluid flows (TSUJI; TANAKA; ISHIDA, 1992), which makes the study of many particulate systems in process engineering possible (ZHU et al., 2008). This includes studies in hydrodynamics of solid and liquid flows interacting with structures and makes it possible to use the method in some areas of naval engineering researches.

Ji et al. (2013) and Lau (2013), for example, simulated the interaction between a ship hull and ice floes to analyze the forces and moments acting on the hull when the ship maneuvers in a broken ice field. Spandonidis and Spyrou (2013) used a discrete element approach to study the flow of a granular media inside a tank of a ship. As presented in Figure 12, different kinds of excitations and motions were used to simulate the roll or yaw motion of ship and then calculate the center of mass of the ship.

Figure 12 - Simulation in DEM of the movement of a granular media (particles) inside a ship tank.

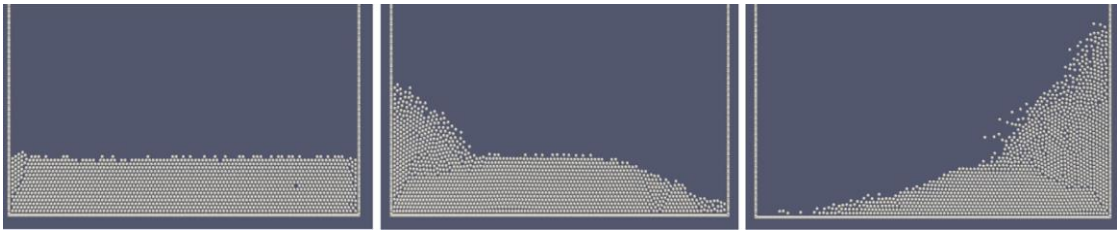

Source: Spandonidis and Spyrou (2013).

In the field of powder technology, the method has been largely used with a variety of ceramic and metals processes and applications, such as compaction, sintering, mechanical tests and fluidized bed processes. Skrinjar ans Larsson (2004) and Martin and Bouvard (2004) studied isostatic and die compaction of a bimodal mixture of powders with different particle sizes and properties and found that mixing

two sizes of particles has a positive effect during the compaction. It was also found that the compression of a mix with large soft spheres and small hard spheres, which is the case of the steel and alumina composite, requires much higher compaction pressures.

Olmos et al. (2008) carried out experiments and simulations on the sintering of copper and alumina composites, and found a big decreasing on densification rate with the increase of alumina fraction in the copper matrix. Bouvard (2000) showed that the relative density of a superalloy and alumina composite decreases significantly with the increasing of ceramic fraction by densifying samples in a hot isostatic press.

Few studies have been using the DEM to simulate bending tests in particulate materials. Nohut (2011) studied the fracture behavior on alumina during four-point test, and found that the crack-tip toughness decreases with increasing grain size. Wolff et al. (2013) carried out simulations of bending tests to find the elastic modulus in beams of alumina particulates bonded with polymer, and found a good agreement with experimental results. The bonding model used in his work is used in the present work to simulate the densified material.

2.3.1. NUMERICAL DESCRIPTION OF DISCRETE ELEMENT METHOD

In the DEM each particle is modelled separately as a solid and indestructible element, which can appreciate rotational and translational movement that results from the interaction with contacting particles or geometries, external applied forces (e.g. gravity), body forces or adhesive particle-particle interactions (e.g. bonding or Van-der-Waals forces). The dynamic information of particles is found by tracing the movements of the individual particles. For each discrete element, the Newton's second law has to solved to determine the translational and rotational motion (POTYONDY; CUNDALL, 2004)**.** In the case of a particle collision, a contact model based on the theory developed by Hertz (1882) for a normal impact, as will be presented later, is used to update the contact force arising from the relative motion of particles.

The simulation in DEM is a dynamic process in which the equations of movement are solved for each particle in each time step. This means that the velocities and accelerations are assumed to be constant within each time step. The definition of a good time step for the simulation is very important. If is set high, disturbances can propagate from a particle farther from the immediate neighbor, and the simulation will not model the real behavior. When is set very low, the computational effort and the simulation time can be impractical.

Thus, for each time step the motion of an individual particle i with mass m_i and volume V_i in the system is calculated using Newton's second law:

$$m_i \frac{\partial \mathbf{v}_i}{\partial t} = m_i \frac{\partial^2 \mathbf{r}_i}{\partial t^2} = \mathbf{F}_i^{tot} \tag{6}$$

$$m_i \frac{\partial \mathbf{v}_i}{\partial t} = \mathbf{F}_i^{tot} = -V_i \nabla p + \frac{V_i \beta}{1-\varepsilon}(u_g - v_i) + m_i g + \sum_{j=1}^{n} F_{c,i,j} + \sum_{k=1}^{m} F_{pp,i,j} \tag{7}$$

Where m_i is the mass, $\mathbf{v}_i$ is the velocity and $\mathbf{r}_i$ the position vector of the particle *i*. $\mathbf{F}_i^{tot}$ represents the sum of the forces acting on the particle, which are shown on the right side of equation 7. They are, respectively from left to right, due to pressure gradient, drag, gravity, contact forces and adhesive forces (SCHILDE; BURMEISTER; KWADE, 2014). The angular momentum is calculated with Euler's equation (8), where $\boldsymbol{\omega}_i$ is the angular velocity and $\mathbf{T}_i^{tot}$ is the total torque acting on the particle, which is the sum of the torques between particle pairs (equation 9) (HEINRICH et al., 2006):

$$I_i \frac{\partial \boldsymbol{\omega}_i}{\partial t} = \mathbf{T}_i^{tot} = \sum_{j \neq 1} \mathbf{T}_{ij} \tag{8}$$

$$\mathbf{T}_{ij} = -\frac{1}{2} \mathbf{r}_{ij} \times \mathbf{F}_{ij} \tag{9}$$

Where $\mathbf{r}_{ij} = \mathbf{r}_i - \mathbf{r}_j$. For the time integration of the equations of motion 6 to 9, the Velocity-Verlet´s propagation algorithm is used as shown in the equations 10 to 12 (HEINRICH et al., 2006).

$$\mathbf{r}_i(t + \Delta t) = \mathbf{r}_i(t) + \Delta t \mathbf{v}_i(t) + \frac{1}{2m}(\Delta t)^2 \mathbf{F}_i^{tot} \quad (10)$$

$$\mathbf{v}_i(t + \Delta t) = \mathbf{v}_i(t) + \frac{1}{2m}\Delta t(\mathbf{F}_i^{tot}(t) + \mathbf{F}_i^{tot}(t + \Delta t)) \quad (11)$$

$$\boldsymbol{\omega}_i(t + \Delta t) = \boldsymbol{\omega}_i(t) + \frac{1}{2I}\Delta t(\mathbf{T}_i^{tot}(t) + \mathbf{T}_i^{tot}(t + \Delta t)) \quad (12)$$

Equations 10 to 12 calculate in sequence of time steps, the new positions, the velocities and the angular velocities of the particles, respectively. In each time step, equations 6 to 12 are going to be solved in a calculation loop, as shown in Figure 13, giving as result the calculated forces, torques and kinematics during the whole simulation. (SALVAGNI, 2013)

Figure 13 - Numerical looping calculation for each time step in a DEM simulation.

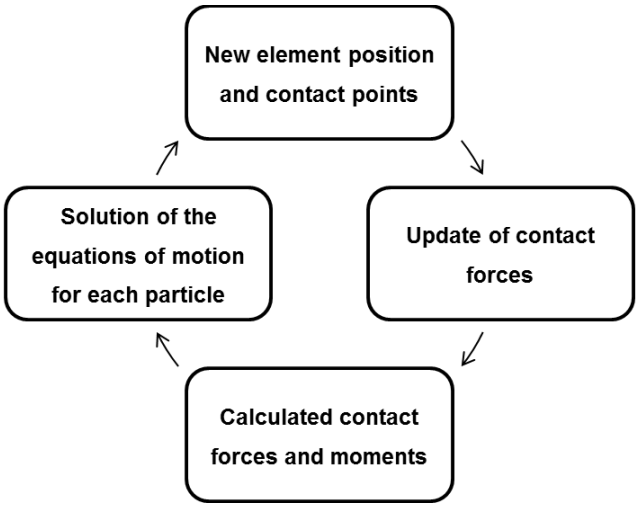

Source: Elaborated by the author.

2.3.2. CONTACT MODEL

In each time step, the DEM update the accelerations, velocities and positions of particles. Therefore, when a particle collision happens, it is necessary to calculate the forces between the particles to update these parameters. To calculate the forces a contac model is necessary. The basic contact model on DEM and used in the present work is the Hertz-Mindlin-Tsuji model.

In this model, the contact forces are divided in normal and tangential direction. The normal force is calculated using a soft-sphere model based on the theory developed by Hertz (1882). A slight deformation of particles is allowed, which means that they can overlap. Multiple contacts between several pairs of particles are possible. For the tangential component of the contact force, a non-slip approximation of the model by Mindlin and Deresiewicz (1953) is used, as proposed by Tsuji, Tanaka and Ishida (1992). (SCHILDE; BURMEISTER; KWADE, 2014)

Figure 14 - Schematic of a collision between two particles.

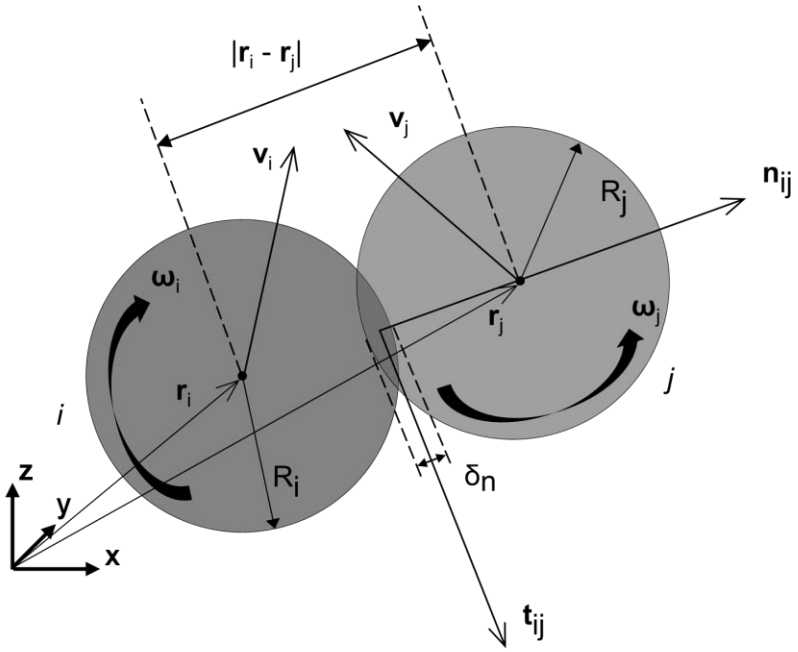

Source: Elaborated by the author.

Consider the two contacting particle *i* and *j* showed in Figure 14, with the position vectors $\mathbf{r}_i$ and $\mathbf{r}_j$ and radii R_i and R_j, respectively. A contact between the two particles is detected when the condition $(R_i + R_j - |\mathbf{r}_i - \mathbf{r}_j| \geq 0)$ is found. The relative velocity $\mathbf{v}_{ij}$ at the contact point is given by:

$$\mathbf{v}_{ij} = (\mathbf{v}_i - \mathbf{v}_j) - (R_i\boldsymbol{\omega}_i - R_j\boldsymbol{\omega}_j) \times \mathbf{n}_{ij} \qquad (13)$$

Where $\mathbf{n}_{ij}$ is the unit vector normal to the contact plane, $\mathbf{v}$ and $\boldsymbol{\omega}$ are the velocities and angular velocities of particles. The normal component of the relative velocity, $\mathbf{v}_{ij,n}$, is defined as:

$$\mathbf{v}_{ij,n} = (\mathbf{v}_{ij} \cdot \mathbf{n}_{ij})\, \mathbf{n}_{ij} \tag{14}$$

The contact between the particles creates an overlap δ_n, which is given by:

$$\delta_n = R_i + R_j - \left|\mathbf{r}_i - \mathbf{r}_j\right| \tag{15}$$

According to the Hertzian theory, the relation between the elastic force and the displacement is nonlinear, due to the elliptical pressure distribution in the circular contact, as is shown (SCHILDE; BURMEISTER; KWADE, 2014):

$$\mathbf{F}_{c,n} = -k_n \cdot \delta_n^{3/2} \cdot \mathbf{n}_{ij} - \eta_n \mathbf{v}_{ij,n} \tag{16}$$

In the DEM model, the elastic part of the normal contact force $\mathbf{F}_{c,n}$ is represented by a non linear spring between the particles (Figure 15), where the force is proportional to the stiffness k_n and the overlap between particles. (SCHILDE; BURMEISTER; KWADE, 2014)

Figure 15 - Equivalent circuit, representing the elastic part of the normal contact force.

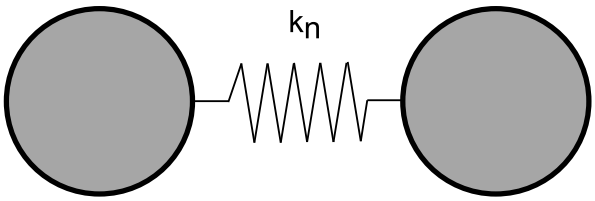

Source: Elaborated by the author.

The stiffness k_n depends on the size and the elastic properties of the particles:

$$k_n = \frac{4}{3} E^* \sqrt{R^*} \tag{17}$$

Where

$$\frac{1}{E^*} = \frac{1 - \nu_i^2}{E_i} + \frac{1 - \nu_j^2}{E_j} \tag{18}$$

$$R^* = \frac{R_i R_j}{R_i + R_j} \tag{19}$$

E^* is the effective modulus of elasticity of the two colliding bodies, which is related with the elastic modulus and the Poisson ratio ν of each element. The median radius R^* of the contact partners is a characteristic radius for the contact surface curvature. (SCHILDE; BURMEISTER; KWADE, 2014)

Figure 16 - Contact between two particles: the spring represents the elastic part of the normal contact force and the dashpot represents the mechanims of energy dissipation.

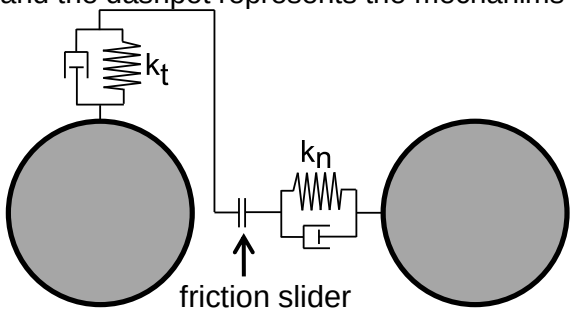

Source: Elaborated by the author.

To account for visco-elastic material properties that cause energy dissipation, a normal damping coefficient η_n is included into the DEM model, as proposed by Tsuji, Tanaka and Ishida (1992)**.** This can be seen as a dashpot between the contacting particles (Figure 16).

$$\eta_n = \begin{cases} \dfrac{-2 \ln e_n \sqrt{m^* k_n}}{\sqrt{\pi^2 + \ln^2 e_n}} & \text{if } e_n \neq 0, \\ 2\sqrt{m^* k_n} & \text{if } e_n = 0, \end{cases} \tag{20}$$

Where m^* is the effective mass of contact partners (equation 21)**,** and e_n the coefficient of normal restitution (equation 22). In particle-wall collisions, the mass of particle *j* (i.e., the wall) is set infinitely large, resulting in $m^* = m_i$. (DEEN et al., 2006)

$$\frac{1}{m^*} = \frac{1}{m_i} + \frac{1}{m_j} \tag{21}$$

The elastic contribution of the impact energy absorbed during the compression is released during the restitution phase of impact and leads to the elastic force that separates the contact partners. The absorption of the kinetic energy during the impact can be described by a restitution coefficient, which is defined as a ratio of the impulse during the restitution phase of impact ($t_c \leq t \leq t_R$) to that during the compression phase ($0 \leq t \leq t_c$) (equation 22). The impulse ratio gives the square root of the elastic strain energy released during the restitution, $W_{kin,R}$, to the impact energy. The restitution coefficient can be obtained experimentally or be aproximated. (ANTONYUK et al., 2010)

$$e = \frac{\int_{t_c}^{t_r} F\,dt}{\int_0^{t_c} F\,dt} = \sqrt{\frac{W_{kin,R}}{W_{kin}}} = \frac{|\mathbf{v}_R|}{\mathbf{v}} \tag{22}$$

In case of a fully elastic impact the impact energy adsorbed during compression is fully restored during the rebound and the relative velocity of contact partners before impact is equal to that after the impact, $e = 1$. In the case of full absorption of initial kinetic energy due to plastic deformation, adhesion, friction in the contact as well as propagation of stress waves, the impact bodies are not separated after the unloading (restitution), $e = 0$. (ANTONYUK et al., 2010)

Two different types of impact, i.e. normal and oblique, are described by normal and tangential restitution coefficients:

$$e_n = \frac{|\mathbf{v}_{n,R}|}{\mathbf{v}_n} \tag{23}$$

$$e_t = \frac{|\mathbf{v}_{t,R}|}{\mathbf{v}_t} \tag{24}$$

Where $\mathbf{v}_n$ and $\mathbf{v}_t$ are normal and tangential components of the velocity vector, respectively. (ANTONYUK et al., 2010)

Figure 17 - Contact between two particles: the springs represents the elastic parts of the normal and tangential contact forces and the dashpots represents the mechanims of energy dissipation. A slider is introduced to represent the frictional force.

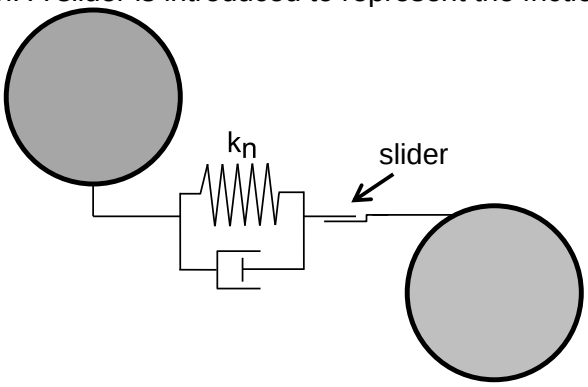

Source: Elaborated by the author.

For the tangential component of the contact force a Coulomb-type friction law is used (equation 25). The force can be represented with a tangential spring/dashpot between the particles, and a slider representing the frictional interaction (Figure 17). When the modulus of the tangential force is higher than the normal force multiplied by the coefficient of friction a relation based on a normal frictional law is used, otherwise, the spring/dashpot law is used.

$$\mathbf{F}_{c,t} = \begin{cases} -k_t\delta_t - \eta_t\mathbf{v}_{ij,t} & \text{if} \quad |\mathbf{F}_{c,t}| \leq \mu|\mathbf{F}_{c,n}|, \\ -\mu|\mathbf{F}_{c,n}|\mathbf{t}_{ij} & \text{if} \quad |\mathbf{F}_{c,t}| > \mu|\mathbf{F}_{c,n}|, \end{cases} \tag{25}$$

Where $\mathbf{v}_{ij,t}$, k_t, η_t, δ_t and μ are the tangencial relative velocity, tangencial spring stifness, tangencial displacement, tangencial damping coefficient and friction coefficient, respectively, and are defined by the follow equations:

$$\mathbf{v}_{ij,t} = (\mathbf{n}_{ij} \times \mathbf{v}_{ij}) \times \mathbf{n}_{ij} \tag{26}$$

$$k_t = 8G^* \sqrt{R^*\delta_n} \tag{27}$$

$$\eta_t = \begin{cases} \dfrac{-2 \ln e_t \sqrt{\dfrac{2}{7} m^* k_t}}{\sqrt{\pi^2 + \ln^2 e_t}} & \text{if } e_t \neq 0, \\ 2\sqrt{\dfrac{2}{7} m^* k_t} & \text{if } e_t = 0, \end{cases} \tag{28}$$

$$\delta_t = \begin{cases} \delta_{t,0}\mathbf{H} + \int_{t0}^{t} \mathbf{v}_{ij,t}\, dt & \text{if } |\mathbf{F}_{c,t}| \leq \mu |\mathbf{F}_{c,n}|, \\ \dfrac{\mu}{k_t} |\mathbf{F}_{c,n}| \mathbf{t}_{ij} & \text{if } |\mathbf{F}_{c,t}| > \mu |\mathbf{F}_{c,n}|, \end{cases} \tag{29}$$

G^* is the equivalent shear modulus of contacting particles:

$$\frac{1}{G^*} = \frac{2 - v_i}{G_i} + \frac{2 - v_j}{G_j} \tag{30}$$

e_t is the coefficient of tangential restitution (equation 24), and **H** is a rotational matrix calculated from the collision angles and geometries. (DEEN et al., 2006)

The contact force between two particles is, therefore, determine by the following parameters: normal and tangential spring stifness k_n and k_t, the coefficient of normal and tangential restitution e_n and e_t, friction coefficient μ and the overlap. The overlap is calculated by the simulation system with the particles positions and movement and the five others parameters must be input in the simulator.

In principle k_n and k_t can be calculated with the elastic modulus and Poisson ration of the solid material. However, in practice their values must be chosen much smaller, otherwise the time step become impractically small. The values for k_n and k_t are thus mainly determined by computational efficiency and not by the material properties. The colission parameters e_n, e_t and μ are typical for the type of particle to be modeled. (DEEN et al., 2006)

2.3.3. THE BONDING MODEL

To simulate the sintering material an approach by a bonding model was used. This model represents solid bonds between particles in contact establishing an elastic interaction between them. It was first introduced to DEM by Potyondy and Cundall (2004) based on the Euler-Bernoulli beam theory, which calculates the forces and moments acting on the bonds by a linear-elastic approach.

A bond can be envisioned as a set of elastic springs uniformly distributed over a circular cross-section lying on the contact plane and centered at the contact point. These springs behave as a beam and can transmit both force and moments between particles (Figure 18). The force–displacement behavior at each bond is described by the following five parameters: normal and shear stiffnesses per unit area, $\bar{k}_n$ and $\bar{k}_t$; tensile and shear strengths, $\bar{\sigma}$ and $\bar{\tau}$; and bond-radius r_b. (POTYONDY; CUNDALL, 2004)

Figure 18 - Representation of a bond between two particles.

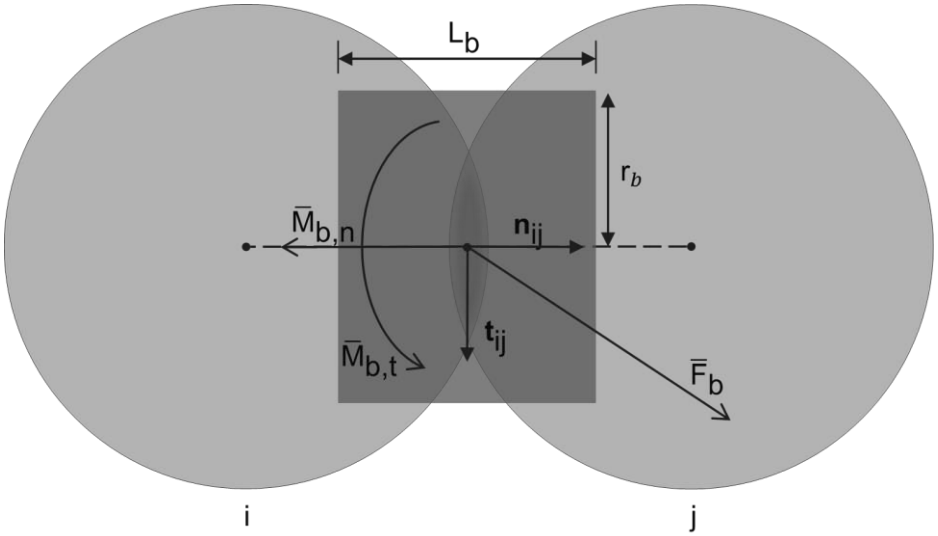

Source: Elaborated by the author.

The total force and moment carried by the parallel bond are denoted by $\bar{F}_b$ and $\bar{M}_b$, respectively. The force and moment vectors can be resolved into normal and tangential components with respect to the contact plane as:

$$\bar{F}_b = \bar{F}_{b,n}\mathbf{n}_{ij} + \bar{F}_{b,t}\mathbf{t}_{ij} \quad (31)$$

$$\bar{M}_b = \bar{M}_{b,n}\mathbf{n}_{ij} + \bar{M}_{b,t}\mathbf{t}_{ij} \quad (32)$$

Where $\bar{F}_{b,n}$, $\bar{F}_{b,t}$ and $\bar{M}_{b,n}$, $\bar{M}_{b,t}$ denote the normal and tangential directed forces and moments, respectively. $\mathbf{n}_{ij}$ and $\mathbf{t}_{ij}$ are the unit vectors that define the contact plane. When the bond is formed, $\bar{F}_b$ and $\bar{M}_b$ are initialized to zero. Each subsequent relative displacement and rotation increment produces an increment of elastic force and moment that is added to the current values. The increments of elastic force and moment are given by:

$$\bar{F}_{b,n} = \bar{k}_n A \Delta\delta_n \quad (33)$$

$$\bar{F}_{b,t} = -\bar{k}_t A \Delta\delta_t \quad (34)$$

$$\bar{M}_{b,n} = -\bar{k}_n J \Delta\theta_n \quad (35)$$

$$\bar{M}_{b,t} = -\bar{k}_t I \Delta\theta_t \quad (36)$$

Where $\Delta\delta_n$, $\Delta\delta_t$ are the overlap increment in normal and tangential directions, respectively ($\Delta\delta_{ij} = \mathbf{v}_{ij}\Delta t$). $\Delta\theta_n$ and $\Delta\theta_t$ are the rotational angles from normal and tangential planes. A, I and J are the area, moment of inertia and polar moment of inertia of the parallel bond cross-section, respectively, and are given by

$$A = \pi r_b^2 \quad (37)$$

$$I = \frac{1}{4}\pi r_b^4 \quad (38)$$

$$J = \frac{1}{2}\pi r_b^4 \quad (39)$$

The maximum tensile and shear stresses acting on the bond periphery are calculated from beam theory, as follow:

$$\bar{\sigma}^{max} = \frac{-\bar{F}_{b,n}}{A} + \frac{\left|\bar{M}_{b,t}\right| r_b}{I} \quad (40)$$

$$\bar{\tau}^{max} = \frac{\left|-\bar{F}_{b,t}\right|}{A} + \frac{\left|\bar{M}_{b,n}\right| r_b}{J} \quad (41)$$

If the maximum tensile stress exceeds the tensile strength or the maximum shear stress exceeds the shear strength, then the parallel bond breaks and it is removed from the model along with its accompanying force, moment and stiffnesses. (POTYONDY; CUNDALL, 2004)

Considering the bond as a cylindrical beam, it is possible to relate the normal stiffness per area with the elastic modulus and the length of the bond:

$$\bar{k}_n = \frac{E_b}{L_b} \tag{42}$$

The Poisson ratio of the bond material then determines the ratio between normal and tangential stiffness:

$$\frac{\bar{k}_n}{\bar{k}_t} = \frac{E_b}{G_b} = 2(1 + \nu) \tag{43}$$

At each time step, the simulator system solves equations 33 to 36, 40 and 41 for each bond. The overlaps and rotational angles are calculated by the software with the particle positions and movements. It is necessary to input the geometry and the stiffness of the bonds. The geometry (radii and length) can be set accordingly the specific bonding required or empirically found. The stiffness can be calculated with the elastic modulus and poisson ratio of the bond material, using equations 42 and 43.

3. EXPERIMENTAL PROCEDURE

In this chapter, the procedures for the virtual experiments are explained. As commented before, the simulations were carried out using a discrete element method. The software used is the EDEM® v 2.5 Academic produced by DEM Solutions Ltd., which is a commercial software and contains all the basic tools necessary to create the particulate structures and carry out the bending tests. The contact model based on the Hertz-Mindlin-Tsuji theory, as it was presented in Chaper 2, is the default model of the software for particle collisions.

The chapter is divided in three sections. First, the properties and geometries used to simulate the steel and alumina particles will be presented, and the steps for compression will be explained. After the generation of the beam, bonding between particles was carried out by using the model presented in Chapter 2. The parameters for this step are presented in the second part.

The third part explains the parameters of bending tests, such as geometries properties, distances and loading velocities.

3.1. Generation of particles and compression

The first step in the simulation is to create the beams by generating and compacting the particles. The material modeled as the discrete particles were: for ceramic the alumina α-Al_2O_3 and for metal the steel 1.2344. Both materials have different properties which are necessary to be input on the software for the calculation of contact forces and for the bonding stiffness.

To simulate the compression, a large box was created involving the particles and then decreased in volume. During this step the shear modulus and coefficient of restitution were set lower to reduce computational effort. Since the focus of the work is on bending tests, the main properties (Table 3) were input correctly just right before the bonding and testing. To ensure that this would not effect the simulation results, the system of particles was left for a certain time without forces acting, to ensure relaxation of all forces. The particles rearrange themselves until a stress-free state of the speciment.

Table 3 - Properties of materials, according to Al-Qureshi (2010).

Properties	**alumina**	**steel**
Density (kg/m^3)	3,980	7,874
Poisson ratio	0.23	0.3
Elastic modulus (GPa)	300	200
Shear modulus (GPa)	169	80

Source: Elaborated by the author.

The physical radius of particles were set to R_{st}= 2.3 µm for steel and R_{al}= 0.3 µm for alumina. Each particle was generated with an additional shell (Figure 19). This shell is created to avoid the physical overlap between particles during the bending tests. A contact would result in additional forces due to the contact model used. However, for the bonding, the model needs a distance value from the center of the particle in which the contact is found.

A shell thickness of 1.2 µm for steel and 0.15 µm for alumina were chosen. The distance from center of the particle is called contact radius (R_i^c) and is the sum of

the physical radius with the shell thickness. Several compression tests were carried out with a lower number of particles to find an optimal shell thickness. This is done to reach a high pack density without residual stresses after compaction and avoid physical overlap.

Figure 19 - Representation of a contact between particles with an additional shell and the difference in sizes between alumina (orange) and steel (blue) particles.

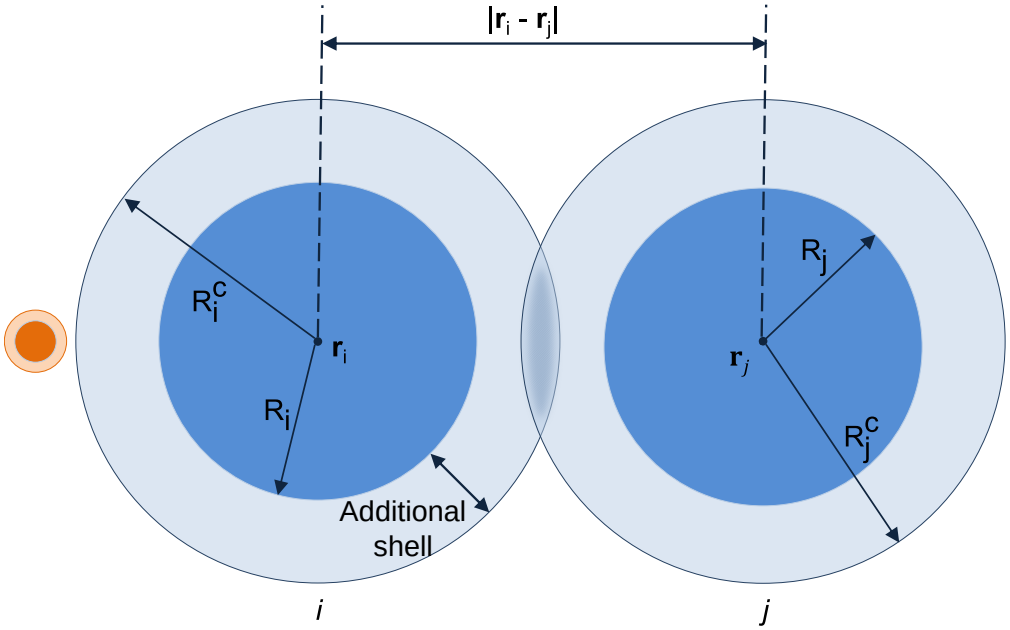

Source: Elaborated by the author.

A contact between two particle *i* and *j* with position vectors $\mathbf{r}_i$ and $\mathbf{r}_j$ and contact radius R_i^c and R_j^c, respectively, is detected when the condition of equation 44 is met (Figure 19).

$$(R_i^c + R_j^c - |\mathbf{r}_i - \mathbf{r}_j| \geq 0) \quad (14)$$

Three compositions of alumina-steel were created, with the following volume fractions of each material:

- 70 vol.% steel + 30 vol.% alumina;
- 50 vol.% steel + 50 vol.% alumina;
- 30v ol.% steel + 70 vol.% alumina.

For each composition the number of steel particles (N_{st}) and alumina particles (N_{al}) is calculated using equations 45 and 46, since they have different sizes and densities:

$$N_{st} = N_{tot} \cdot X_{st} \quad (45)$$

$$N_{al} = N_{tot} \cdot X_{al} \quad (46)$$

Where N_{tot} is the total number of particles, X_{st} and X_{al} are the fraction of particles of steel and alumina and can be calculated as follows:

$$X_{st} = \frac{\frac{\varphi_{st}}{V_{st}}}{\left(\frac{\varphi_{st}}{V_{st}} + \frac{\varphi_{al}}{V_{al}}\right)} \quad (47)$$

$$X_{al} = \frac{\frac{\varphi_{al}}{V_{al}}}{\left(\frac{\varphi_{st}}{V_{st}} + \frac{\varphi_{al}}{V_{al}}\right)} \quad (48)$$

Where φ_{st} and φ_{al} are the volume fractions of steel and alumina, V_{al} and V_{st} are the particles volumes, which for a sphere is:

$$V = \frac{4}{3}\pi R^3 \quad (49)$$

Table 4 presents the numbers of particles generated for each composition. For the composition with 70 vol.% steel two samples were simulated: one with 10,000 particles and other with 100,000. The samples with 50 and 30 vol.% steel were generated with 100,000 particles. It is possible to see a very big difference in number of particles of alumina and steel because of the difference in size.

Table 4 - Number of particles generated for each composition.

Composition (vol.% steel)	N_{st}	N_{al}
70 (N_{tot}= 10,000)	50	9950
70 (N_{tot}= 100,000)	493	99507
50 (N_{tot} = 100,000)	212	99788
30 (N_{tot} = 100,000)	91	99909

Source: Elaborated by the author.

The particle size distributions obtained are presented in Figure 20. The size distribution range of the real powder is wider than the simulated ones. In the simulation a narrow distribution was used to save computational effort. The average particle diameter of the alumina distribution is very similar to the real powder. For the steel an average particle size 10% smaller was used in the simulation.

The packing density ρ_p was determined in the following way: first a cuboid of certain size was defined within the specimen. The volume of all particles whose centres were located within this volume were summed up and this was divided by the total volume of the chosen cuboid. This was done for several cuboid sizes on different positions and the resulting average packing densities are presented in Table 5. The effect of the surface on the packing density could be eliminated and the true bulk density was determined. (WOLFF et al., 2013)

Figure 20 - Cumulative particle size distributions of alumina and steel for real and simulated cases.

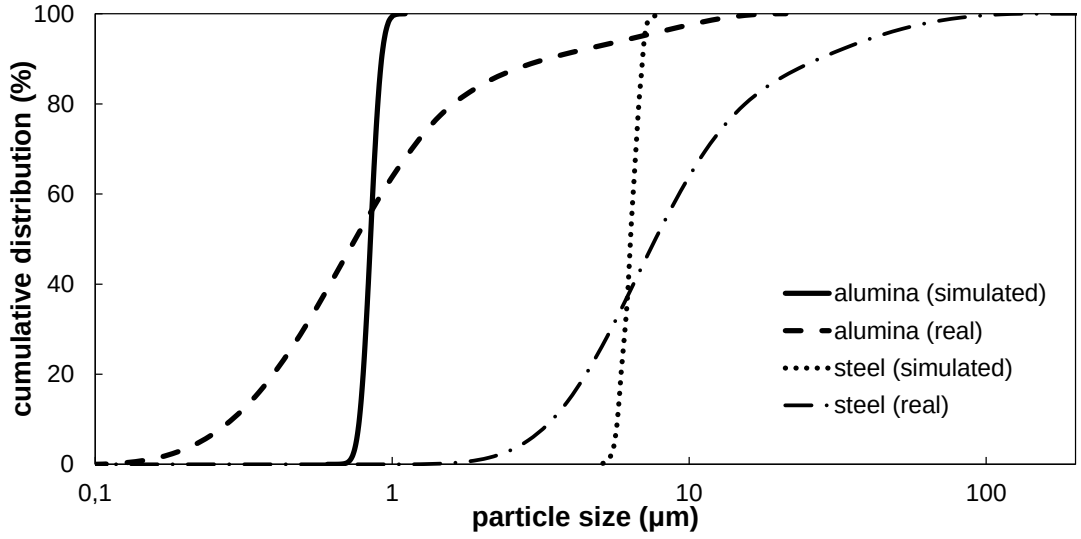

Source: Elaborated by the author.

Table 5 - Geometries and packing densities of generated beams.

Composition (vol.% steel)	Length (L_{beam},µm)	Width (w,µm)	Height (h,µm)	Packing density (ρ_p)
70 (N_{tot} = 10,000)	92.6	9.2	10	65.8%
70 (N_{tot} = 100,000)	276	23.6	24.1	63.5%
50 (N_{tot} = 100,000)	223.9	20	20.4	66.3%
30 (N_{tot} = 100,000)	212	18	19	60.5%

Source: Elaborated by the author.

3.2. Bonding

To calculate the forces acting on the bonds, the simulation system needs the elastic modulus, poisson ratio and geometry of bonds. The objective was to simulate the sintered material, in which the bonding is done by the same material of the particles. Therefore, the parameters were calculated according to the materials properties (Table 3). Bonds between steel-steel and alumina-alumina were generated and the input parameters are presented in Table 6. For the steel-alumina contacts no bonding was created and the frictional and contact forces acting between them are the only considered during the bending tests.

Table 6 - Input parameters for the bonding.

Bond	$\bar{k}_n$ (N/m^3)	$\bar{k}_t$ (N/m^3)	r_b (µm)	L_b (µm)
alumina - alumina	$3.33 \cdot 10^{17}$	$1.35 \cdot 10^{17}$	0.45	0.9
steel - steel	$2.86 \cdot 10^{16}$	$1.1 \cdot 10^{16}$	3.5	7

Source: Elaborated by the author.

Table 7 presents the total numbers of bonds created for each particle contact. A big decrease in steel bonds with the different compositions can be seen. In samples with 70, 50 and 30 vol.% steel, the average coordination numbers (CN) for

steel are 4.7, 3.6 and 2, respectively. For alumina, they are 4.3, 5.6 and 6,1, considering only contacts between particles of the same material.

Table 7 - Numbers of bonds and contacts between particles.

Composition (vol.% steel)	Bonds Al_2O_3 - Al_2O_3	Bonds steel - steel	Contacts steel - Al_2O_3
70 ($N_{tot} = 10{,}000$)	52,184	136	12,976
70 ($N_{tot} = 100{,}000$)	426,720	2,339	210,011
50 ($N_{tot} = 100{,}000$)	562,194	771	142,892
30 ($N_{tot} = 100{,}000$)	610,404	187	73,185

Source: Elaborated by the author.

3.3. Flexural tests

The four-point bending test was simulated for all samples. Four cylinders were created with different geometries and distances for each composition (Table 8). The density of the cylinder material was set to 10,000 kg/m^3, the poisson ratio to 0.25 and the shear modulus to 169 GPa, same as alumina.

Table 8 - Geometries and loading velocities of the cylinders for bending tests.

Composition (vol.% steel)	Radius of cylinders (μm)	Distance between lower cylinders (L,μm)	Loading speed (m/s)
70 ($N_{tot} = 10{,}000$)	3	80	0.1
70 ($N_{tot} = 100{,}000$)	10	240	1, 0.5
50 ($N_{tot} = 100{,}000$)	10	200	1
30 ($N_{tot} = 100{,}000$)	10	180	1

Source: Elaborated by the author.

All tests were carried out with $a = 0.25\,L$, same used in physical experimental tests for this material. The loading speeds, which is the descent velocity of upper cylinders, were set relatively high comparing to realistic tests. However no big

influence is expected, since the time step used during the simulations is relatively small, with the value of $1 \cdot 10^{-11}$ s. (WOLFF et al., 2013)

The time step, which is the amount of time between two successive iterations, is calculated with the rayleigh time step. In definition, the rayleigh time step is the time taken for a shear wave to propagate through a solid particle. Therefore, it is a theoretical maximum time step for a DEM simulation of a quasi-static particulate collection in which the coordination number for each particle remains above 1. The smaller the time step, the more data points are produced. A large number of data points produce results with a very fine level of detail, however the simulation time will be longer due to the increased number of calculations required. The rayleigh time step is given by:

$$T_r = \frac{\pi R \left(\frac{\rho}{G}\right)^{1/2}}{(0.1631\nu + 0.8766)} \tag{50}$$

Where R is the particle's radius, ρ its density, G the shear modulus and ν the poisson ratio. In practice some fraction of this maximum value is used and for high coordination numbers (4 and above) a typical time step of $0.2T_r$ (20%) has been shown to be appropriate. When using a simulation with a range of particle sizes, the rayleigh time step is calculated based on the smallest particle size. (DEM SOLUTIONS)

After the correct setting of properties and before bonding, the particles were left to rearrange until a stress-free state was found. Therefore, no effect on particle distribution or on bending tests are expected because of the compression process.

Table 9 - Material parameters used for the bonding and bending tests.

Interactions	Coefficient of Restitution	Coefficient of Static Friction	Coefficient of Rolling Friction
alumina - alumina	0.8	0.1	0.01
alumina - steel	0.8	0.5	0.3
steel - steel	0.8	0.1	0.01
particles - geometry	0.0001	0.0001	0.00001

Source: Elaborated by the author.

Table 9 presents the coefficients of friction and restitution for contacts between particles and particle-gemoetry. The coefficients for particle-geometry interactions were set low during the testing phase, in order to prevent the bouncing of the sintered body or particles when the collision between them and the cylinders occurs. The coefficient of friction between alumina and steel were set higher than between particles of same material, since no bonding was created and the frictional forces are expected to be higher. Figure 21 shows a final sample with 70 vol.% steel after the bonding and ready for the bending test.

Figure 21 - Sample with 70 vol.% steel (gray particles) + 30 vol.% Al_2O_3 (yellow particles) after bonding with the cylinders positioned for the bending tests.

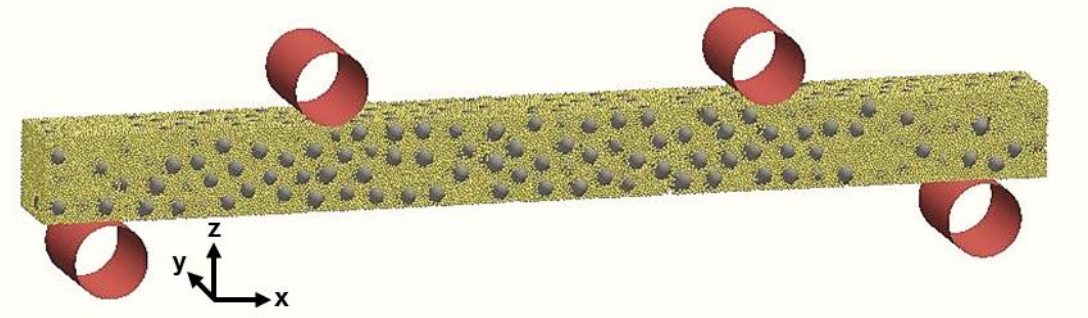

Source: Elaborated by the author.

4. RESULTS

In this chapter the results of the simulations will be presented, with an analysis and discussion, comparing with results of real tests. The first part presents the distribution of particles within the beam. This is an important point since the particles simulated have a big size ratio and the mechanical behavior can vary significantly when the distribution is not random. The structure formed in the simulations by interconnected particles is compared with the real microstructure of the composite.

The second part treats about the results on the mechanical properties and behavior of the material during the bending tests. The tension-compression areas in the beams and the force-displacement curves obtained are presented. The elastic modulus is calculated and compared with real experimental results.

4.1. Distribution of particles within the beam

4.1.1. SAMPLES WITH 70 VOL.% STEEL

Figure 22 presents a sample with 70 vol.% steel and N_{tot} = 10,000 particles. In Figure 23, the diameter of alumina particles is ploted as a fuction of beam length, width and height. The blue dots represent the centres of alumina particles.

In Figure 23b and 23c, two discrete levels are visible near each surface of the beam (maximum magnitude of y and z). The two outmost levels which limit the width and height of the beam are slightly inclined. This is because for the given constraint of a smooth surface the centre of larger particles cannot be located equally far away the surface as the centre of smaller particles. By going away from the surface into the beam (smaller magnitude of y and z), the effect of the surface averages out, and a random packing is established. Such surface effect is not visible in the x direction distribution (Figure 23a), since the length of the beam is much bigger. Large and small particles are statistically homogeneously distributed within the beam.

By considering these aspects, a random packing of particles in the interior of the beam can be assumed. However, in the case of N_{tot} = 10,000 particles, the coordination number and the ratio between beam height and steel particle diameter is very low (h/d_{st} ~ 1.43). This causes a significant effect on the tests, since the interconnected network formed by the steel particles bonded is small. This point is solved by using a higher number of particles, as will be shown later.

Figure 22 - Sample with 70 vol.% steel (gray) + 30 vol.% alumina (yellow) and N_{tot} = 10,000, sliced in its width.

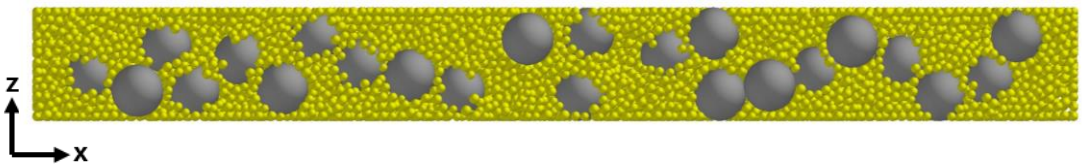

Source: Elaborated by the author.

Figure 23 - Distribution of alumina particles in x direction (a), y direction (b) and z direction (c) as function of particle diameter, for the sample with 70 vol.% steel and N_{tot} = 10,000 particles, before loading.

(a)

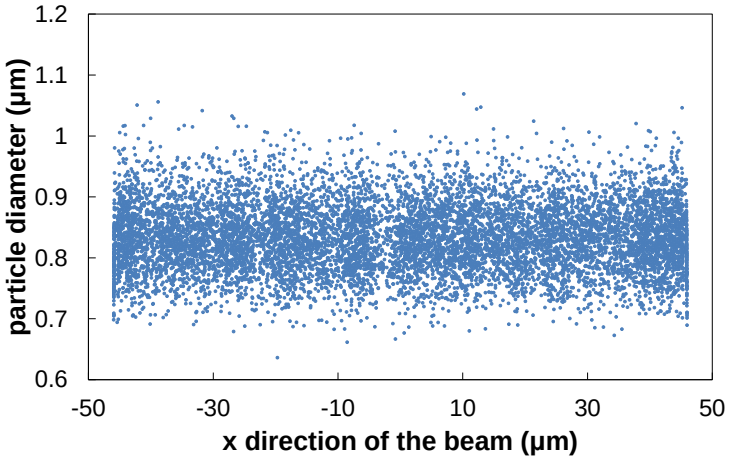

(b)

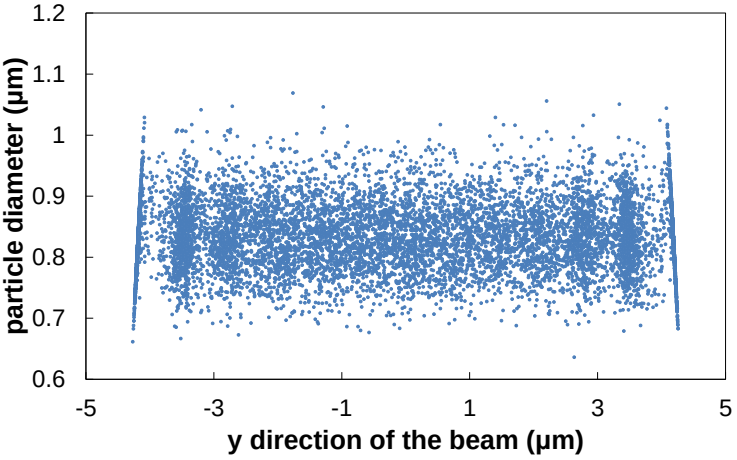

(c)

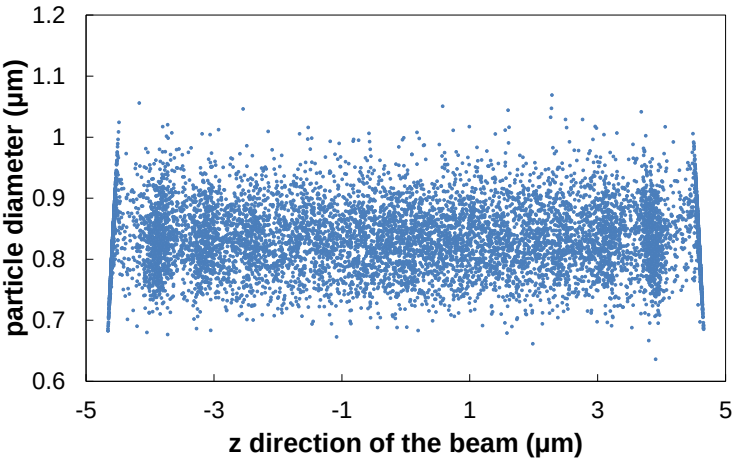

Source: Elaborated by the author.

The distributions of particles in x,y and x,z planes are presented in Figure 24, after bonding. The red dots are the centres of steel particles. A random distribution of steel particles is visible and also the surface effect on the high magnitude of y and z

with the alumina particles. In the interior of the beam, some areas where less alumina particles are found. This volume is occuppied by the relatively big steel particles.

Figure 24 - Distribution of alumina and steel particles: (a) in x,y plan and (b) x,z plan after the bonding and before loading, for the sample with 70 vol.% steel and N_{tot} = 10,000 particles.

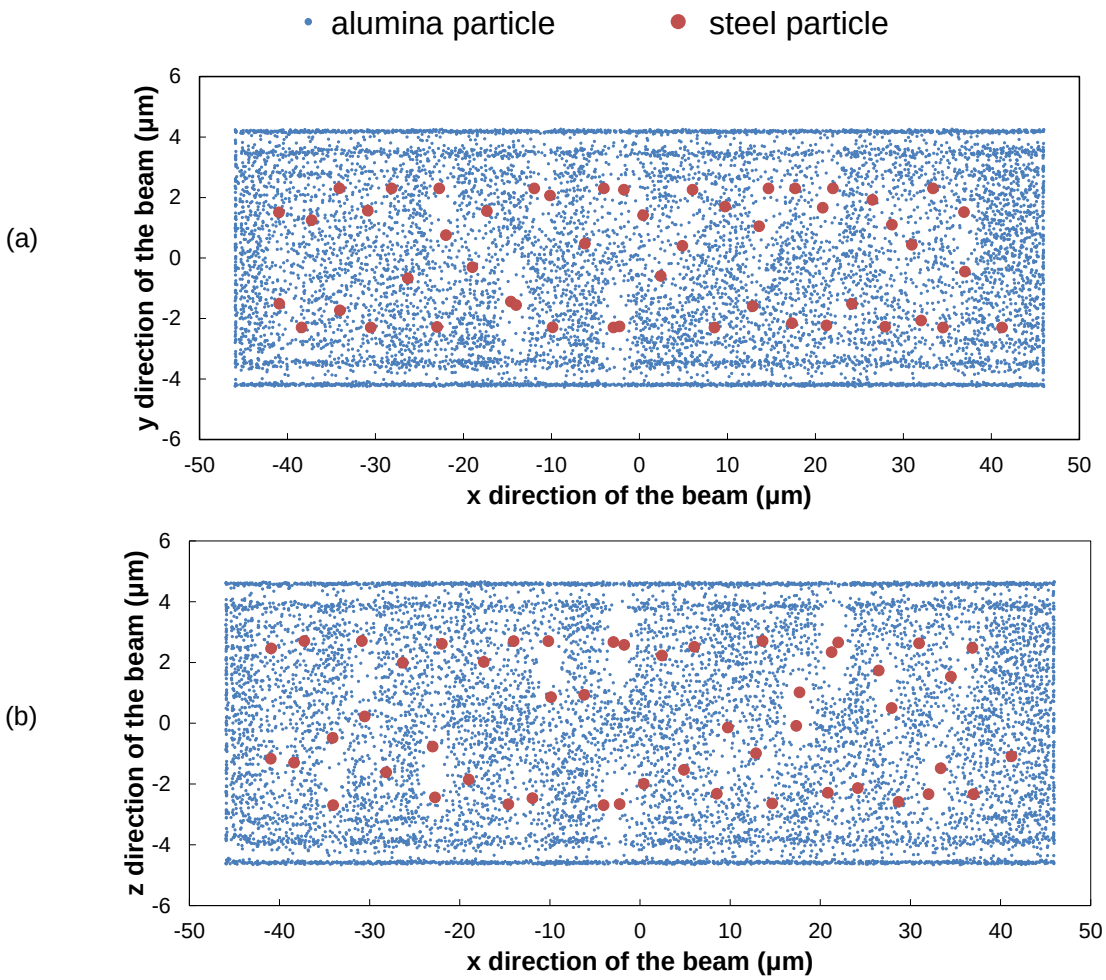

Source: Elaborated by the author.

Figure 25 presents the distribution of alumina and steel particles in x, y and z directions as function of particle diameter for the sample with 70 vol.% steel and N_{tot}= 100,000 particles. In this case, the surface effect is present also with the steel particles, which are in a higher number. The two outmost levels which limit the width and height of the beam are inclined, because the constraint of a smooth surface. The center of steel particles are located far from the surfaces. A random distribution can be expected since the particle diameter of steel is relatively big. The particles located near the surface are in contact with the particles in the interior of the beam. In Figure 25a the random distribution within the length of the beam is clearly visible.

The constraint effect of smooth surface on alumina distributions does not have a significant impact on the distribution as have for the sample with N_{tot} = 10,000 particles. A higher number of particles is simulated. Therefore, a random distribution can be achieved.

Figure 25 - Distribution of steel and alumina particles in x direction (a), y direction (b) and z direction (c) as function of particle diameter, for the sample with 70 vol.% steel and N_{tot} = 100,000 particles, before the loading.

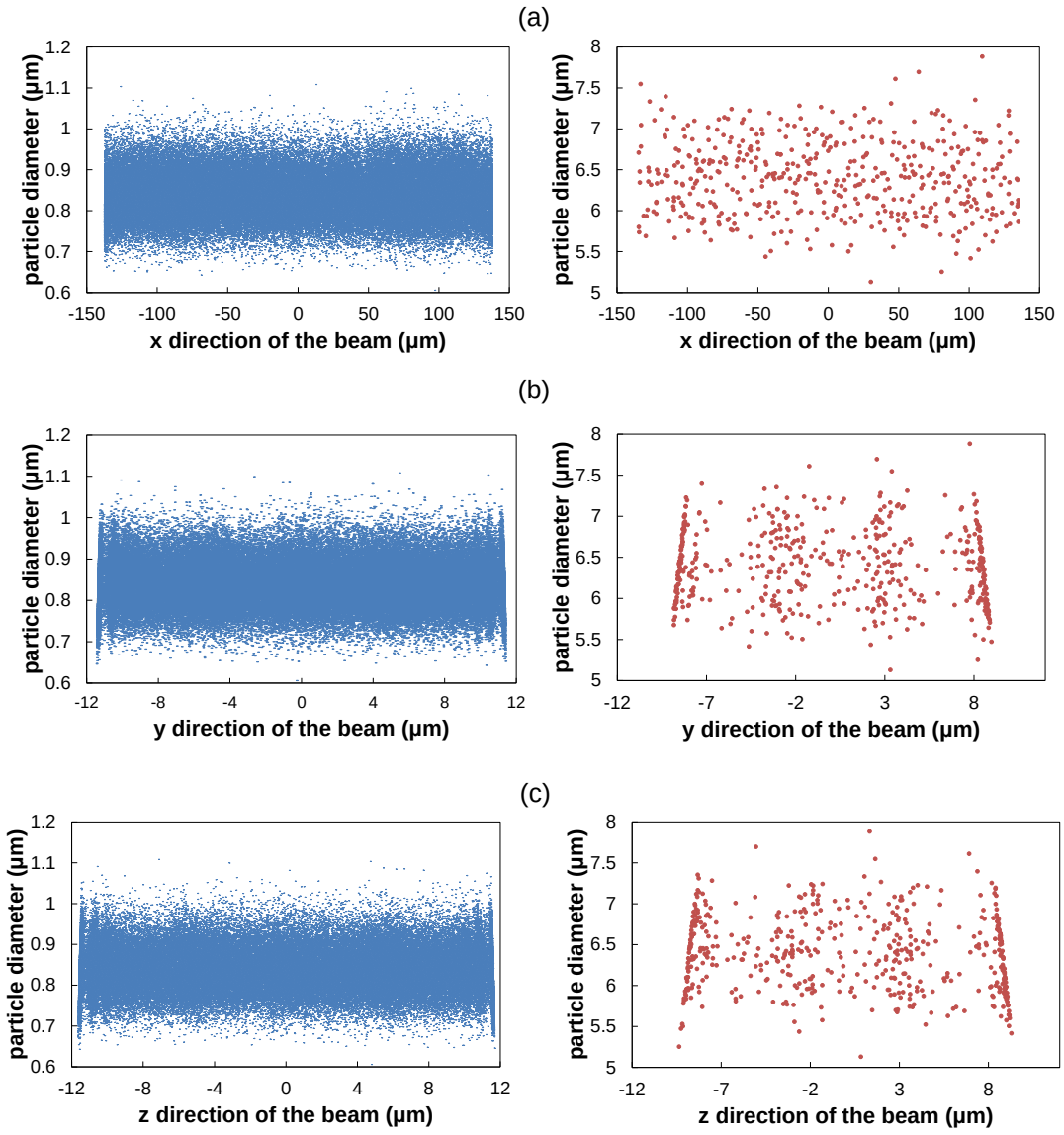

Source: Elaborated by the author.

The distributions along length, width and height are presented in Figure 26, after the bonding. Four discrete levels of steel particles within width and height are visible. Since the particle diameter is big, the particles of one level are in contact with

particles on the closest levels. However, since the ratio between particle diameter and the beam height and width are higher ($h/d_{st} \sim 3.45$ and $w/d_{st} \sim 3.37$), a random distribution is expected. The constraint surface effect is visible on alumina particles within width and height.

Figure 26 - Distribution of alumina and steel particles: (a) in x,y plan and (b) x,z plan, after bonding and before loading, for the sample with 70 vol.% steel and N_{tot} = 100,000 particles.

(a)

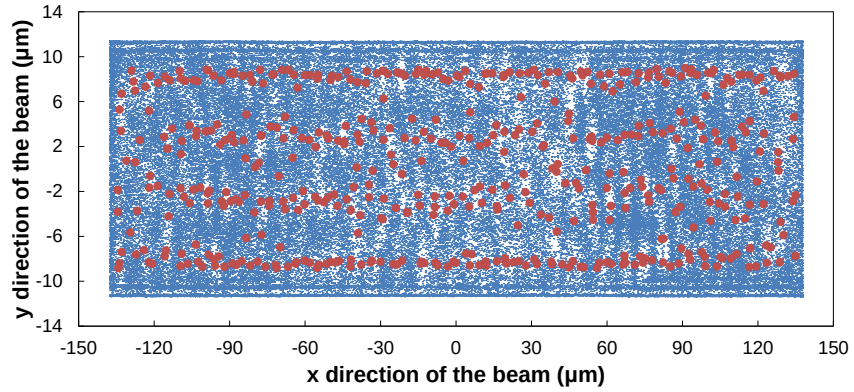

(b)

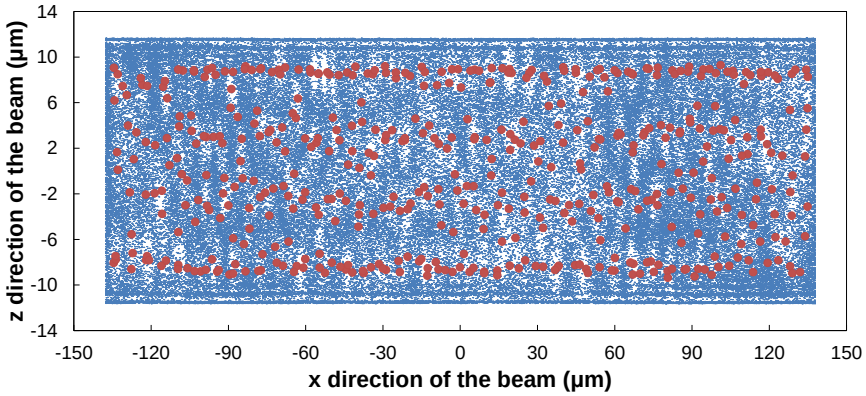

Source: Elaborated by the author.

In Figure 27a and b, the sample with 70 vol.% steel and N_{tot}= 100,000 particles is presented sliced in its width. The discrete levels of steel particles are not visible, but a random packing in all directions. For this composition, the steel can be considered the matrix and the alumina as the interpenetrating structure. Figure 27 presents in a higher magnification the structure of the beam. It is possible to see that the steel is strongly connected and a big network is formed. Meanwhile, the alumina particles form big aggregates in the space between the steel particles. These aggregates are connected between themselves and it is possible to consider that a network is formed.

Figure 27c presents the microstructure of a real sample and the interconnected network formed by steel (white) is clearly visible. The alumina

particles (black) form big aggregates, which are not strongly connected between themselves. At this volume fraction, it is not possible to say that the alumina is percolated. However, the limit from the aggregates situation to percolation is very close.

Figure 27 - (a) simulated sample with 70 vol.% steel (gray) + 30 vol.% alumina (yellow) and N_{tot}= 100,000 particles, sliced in its width, (b) microstructure formed on the simulated sample showing alumina aggregates and steel particles, and (c) microstructure obtained by SEM of a real sample showing the steel network (white) and alumina aggregates (black).

(a)

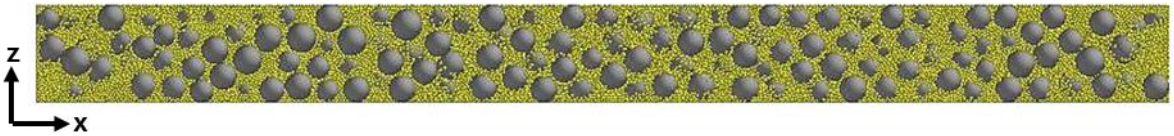

(b)

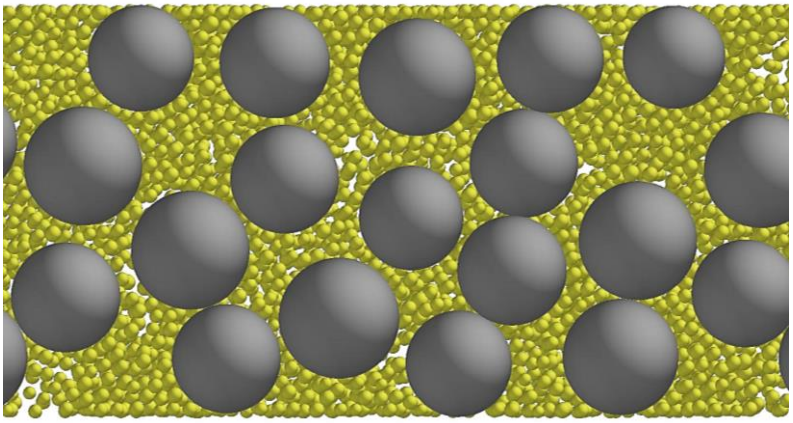

(c)

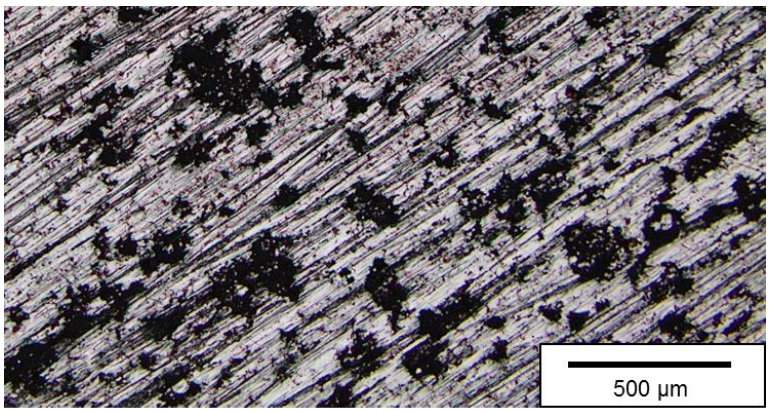

Source: Elaborated by the author.

4.1.2. SAMPLE WITH 50 VOL.% STEEL

In Figure 28, the diameter of alumina and steel particles is plotted as a fuction of beam length, width and height, for a sample with 50 vol.% steel and N_{tot}= 100,000 particles.

Figure 28 - Distribution of alumina particles in x direction (a), y direction (b) and z direction (c) as function of particle diameter, for the sample with 50 vol.% steel and N_{tot} = 100,000 particles, before the loading.

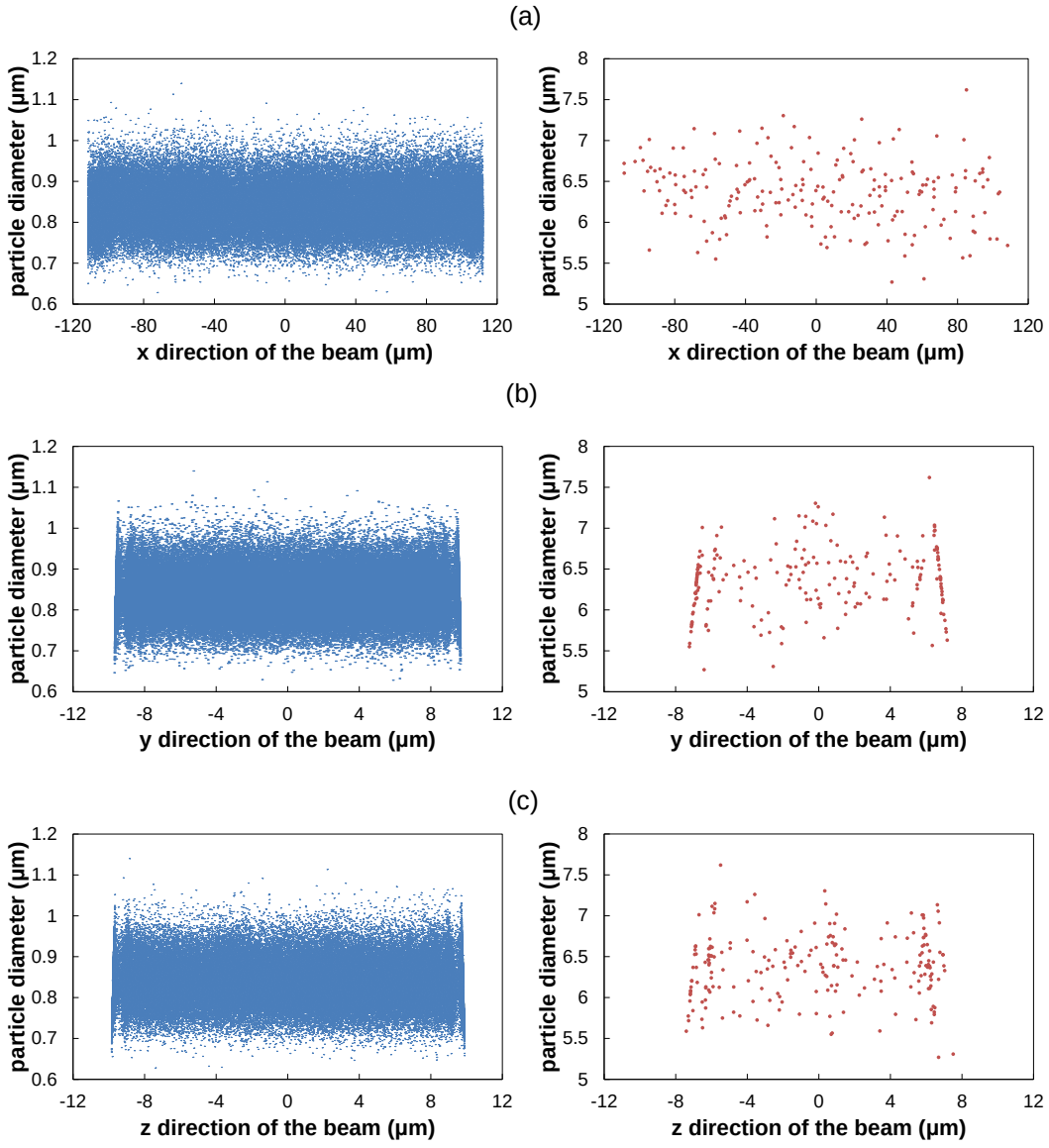

Source: Elaborated by the author.

Within the length, a random distribution is clearly visible (Figure 28a). A constraint effect of smooth surface on steel particles is still present within width and height. However, in the interior of the beam no discrete levels are formed since the number of particles is lower. For the alumina, a small constraint effect of surface is present within height and width, but the random distribution is predominant.

Figure 29 presents the distributions of particles in x,y and x,z planes, before and after the bending. In this case, three discrete levels of steel particles are visible, two near the surfaces and one near the middle. The particles of one level are in contact with particles on the closest levels. Considering the ratio of particle diameter with heigth and width ($h/d_{st} \sim 2.91$ and $w/d_{st} \sim 2.86$), a random distribution is expected. For the alumina, a surface effect is visible within width and height. A random distribution is predominant in the interior of the beam.

Figure 29 - Distribution of alumina and steel particles: (a) in x,y plan and (b) x,z plan, after bonding and before loading, for the sample with 50 vol.% steel and N_{tot} = 100,000 particles.

(a)

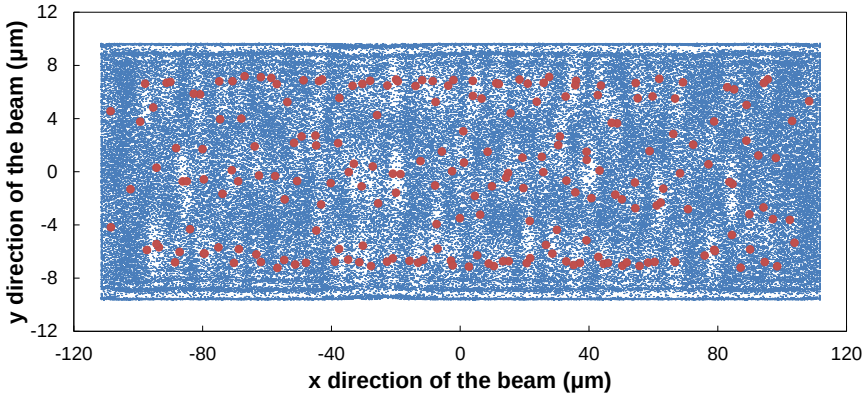

(b)

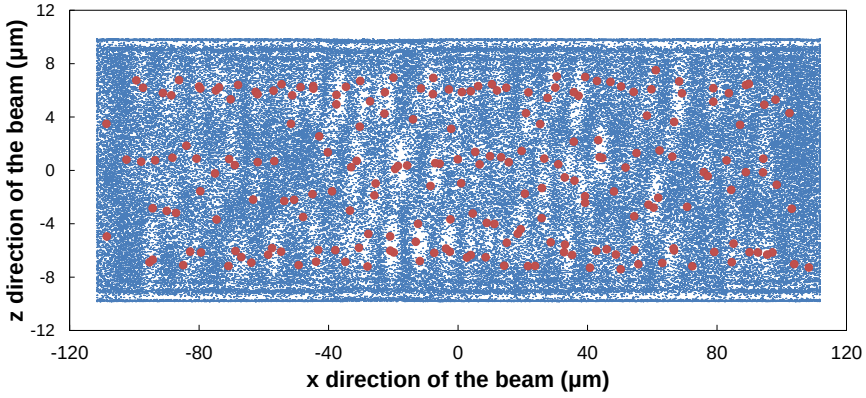

Source: Elaborated by the author.

In Figure 30a, where the simulated sample is sliced in its width, a random distribution is visible. Both steel and alumina form a network of interconnected aggregates in the structure, as can bee seen in Figure 30b. The alumina forms bigger agglomerates which are connected between each other by three or four bonded particles. This creates a stronger structure of alumina. With 50 vol.% steel, it is not possible to affirm which material is the matrix and which is the inclusion. A similar behavior is found on the microstructure of a real sample (Figure 30c).

Figure 30 - (a) simulated sample with 50 vol.% steel (gray) + 50 vol.% alumina (yellow) and N_{tot}= 100,000 particles, sliced in its width, (b) microstructure formed on the simulated sample showing the alumina and steel aggregates network, and (c) microstructure obtained by SEM of a real sample showing the steel network (white) and alumina network (black).

(a)

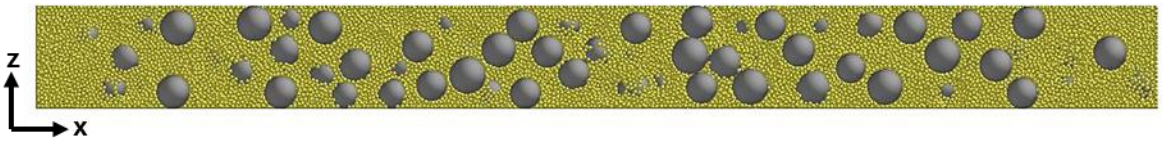

(b)

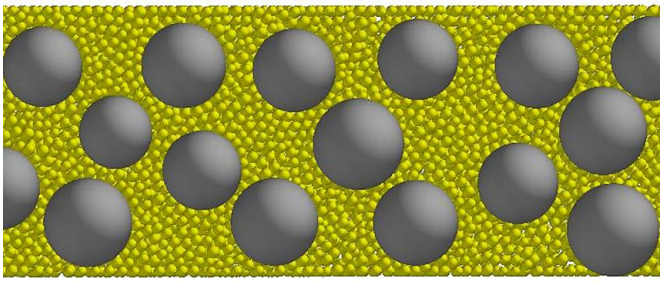

(c)

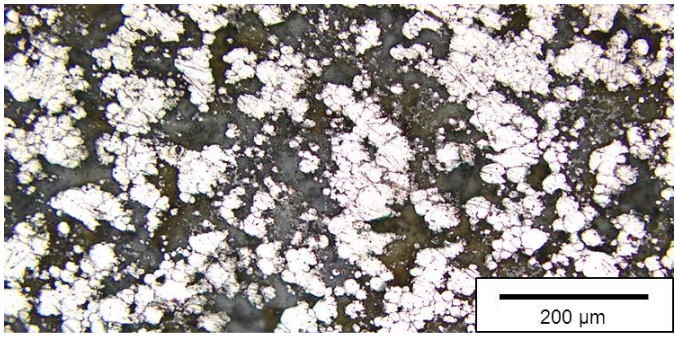

Source: Elaborated by the author.

4.1.3. SAMPLE WITH 30 VOL.% STEEL

The distributions of alumina and steel particle diameter as a function of beam length, width and height, are presented in Figure 31 for a sample with 30 vol.% steel and N_{tot}= 100,000 particles. The distributions of alumina particles are very similar to the samples with 70 and 50 vol.% steel. The steel distributions are random. The discrete levels of steel particles are not visible. This is because the number of steel particles is much lower. The constraint effect of smooth surface is clearly visible only for alumina particles.

Figure 31 - Distribution of alumina particles in x direction (a), y direction (b) and z direction (c) as function of particle diameter, for the sample with 30 vol.% steel and N_{tot} = 100,000 particles, before the loading.

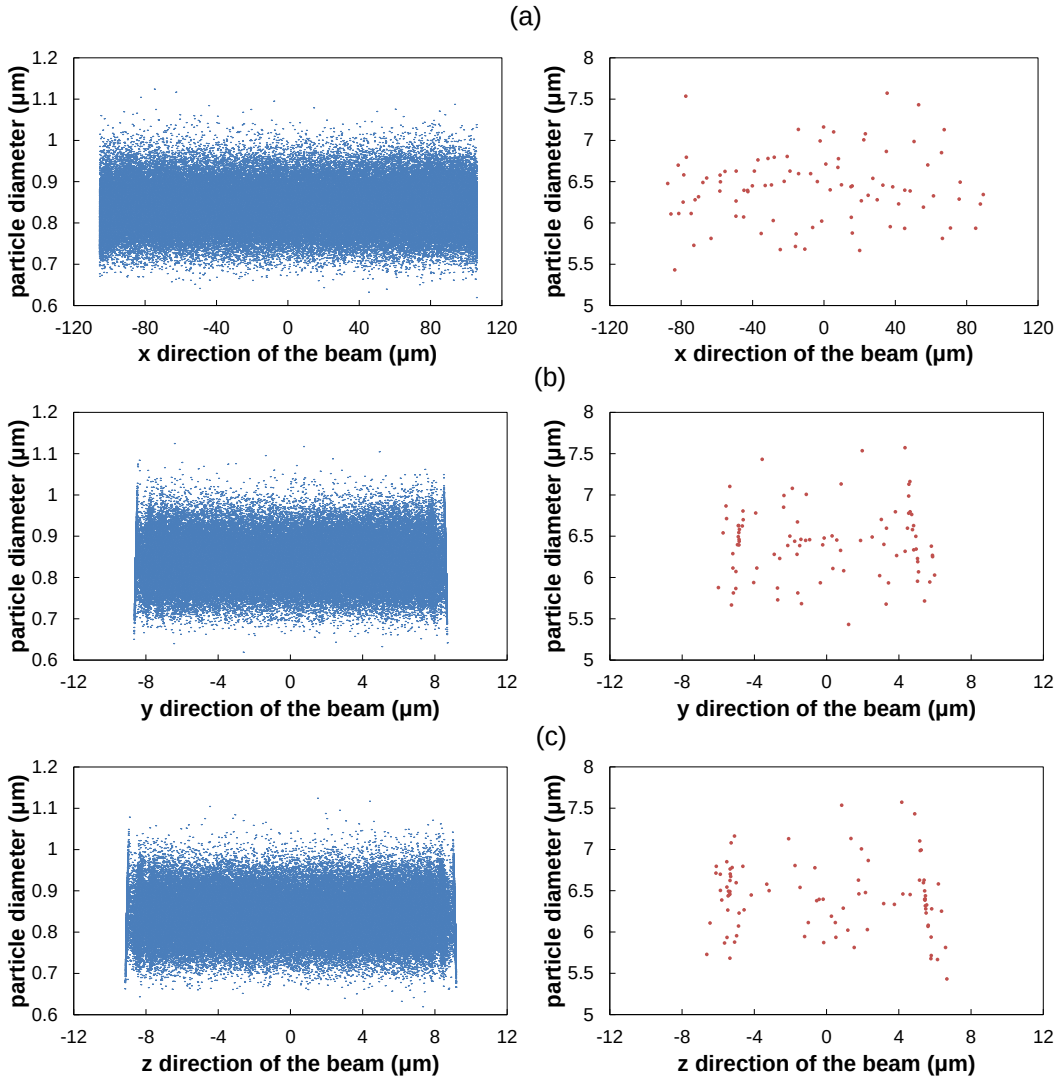

Source: Elaborated by the author.

Figure 32 presents the distributions of particles in x,y and x,z planes, after the bonding. The discrete levels of steel particles are not clearly visible, since the number of particles is lower. Near the length edges, the number of steel particles is practically zero. The alumina particles form a discrete level on the surface and in the interior a random distribution is found.

Figure 32 - Distribution of alumina and steel particles: (a) in x,y plan and (b) x,z plan after bonding and before loading, for the sample with 30 vol.% steel and N_{tot} = 100,000 particles.

(a)

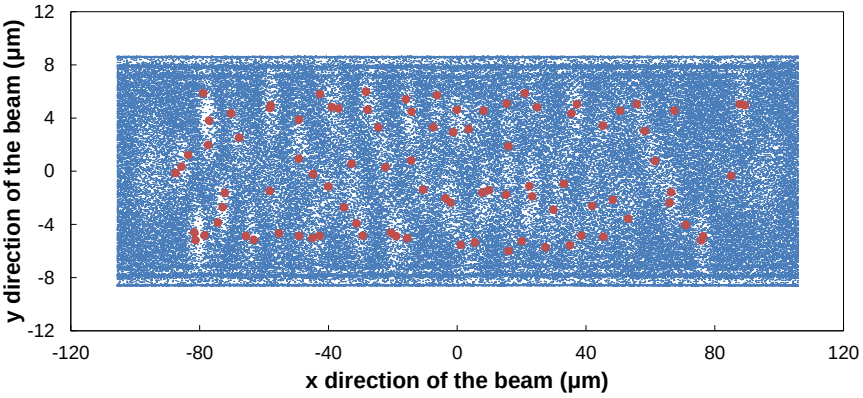

(b)

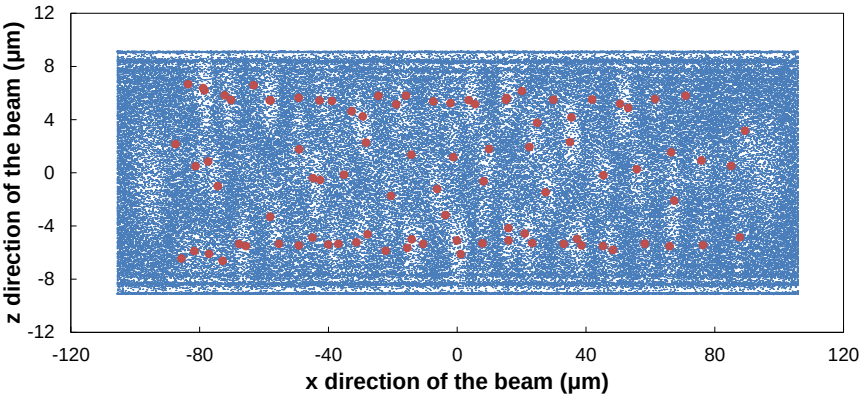

Source: Elaborated by the author.

Figure 33a shows that the particles are randomly distributed within the beam. In this case, alumina is considered the matrix and the steel particles the inclusion material. They form small agglomerates (Figure 33b). Similar structure is visible in Figure 33c, which shows the microstructure of a sample with 30 vol.% steel. The small steel agglomerates or individual particles are visible inside the alumina matrix. At this fraction, the material can be considered as a particulate composite.

Figure 33 - (a) simulated sample with 30 vol.% steel (gray) + 70 vol.% alumina (yellow) and N_{tot}= 100,000 particles, sliced in its width, (b) microstructure formed on the simulated sample showing the alumina matrix and the steel particles, and (c) microstructure obtained by SEM of a real sample showing the steel small aggregates (clear) and alumina matrix (dark).

(a)

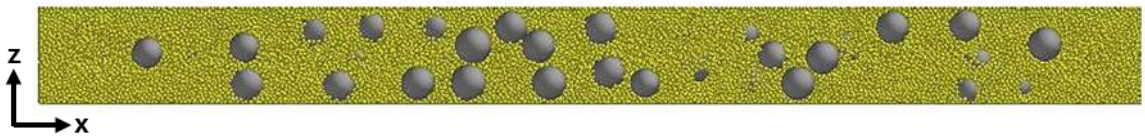

(b)

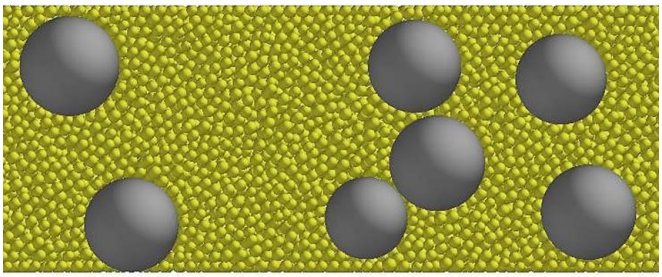

(c)

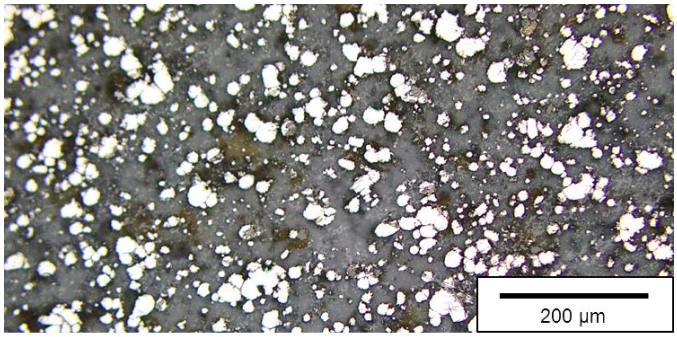

Source: Elaborated by the author.

4.2. Mechanical properties during flexural tests

After the compression and bonding, the resulting specimens had a length on the 10^2 µm-scale, which is about two orders of magnitude smaller than typical sample sizes for mechanical bending tests (cm-scale). However, while the strength of brittle materials typically decreases with the sample size, no appreciable dependence of the modulus of elasticity on the sample size is expected for the composite structure within this size range. (WOLFF et al, 2013)

4.2.1. TENSION-COMPRESSION BEHAVIOR

The bending tests were carried out on the samples with 70 vol.% steel. During the loading, the two lower supports were capped and the upper cylinders were moved at constant speed downwards. Figure 34 presents the loading of the beams. For the sample with N_{tot} = 10,000 particles, a loading speed of 0.1 m/s was set, and for the sample with N_{tot} = 100,000 particles two tests were carried out, one at 1 m/s and one at 0.5 m/s. The blue color indicates the compressive load and the red color corresponds to tensile load.

Figure 34 shows that the lower part of the beams is in tension while the upper part is in compression. A neutral axis in the middle of the beam is formed in some parts. Since the steel particles are big, they have a significant influence and a straight axis is not possible to be formed. Some areas with less or no stress are visible in upper and lower parts and areas of tension or compression in the middle of the beam. This is because the bonding was not created between steel and alumina particles.

In the sample with N_{tot} = 100,000 particles, very similar areas of stresses on tests with different loading speeds are visible. This means that no big influence on the results can be expected with varying the loading speeds.

A very interesting behavior is noted with some alumina particles in contact with steel. In areas where compression stresses were expected, some particles are in

tension, and the oppossite also occurs in areas where tension was expected. This can be seen in Figure 34 as the red spots in the upper part of the beams or the blue spots in the lower part. This happens because of the atrittion forces between them. A detailed analysis of this case will be done later.

Figure 34 - Compressive force on particles during the bending tests on samples with 70 vol.% steel for different N_{tot} and load velocities.

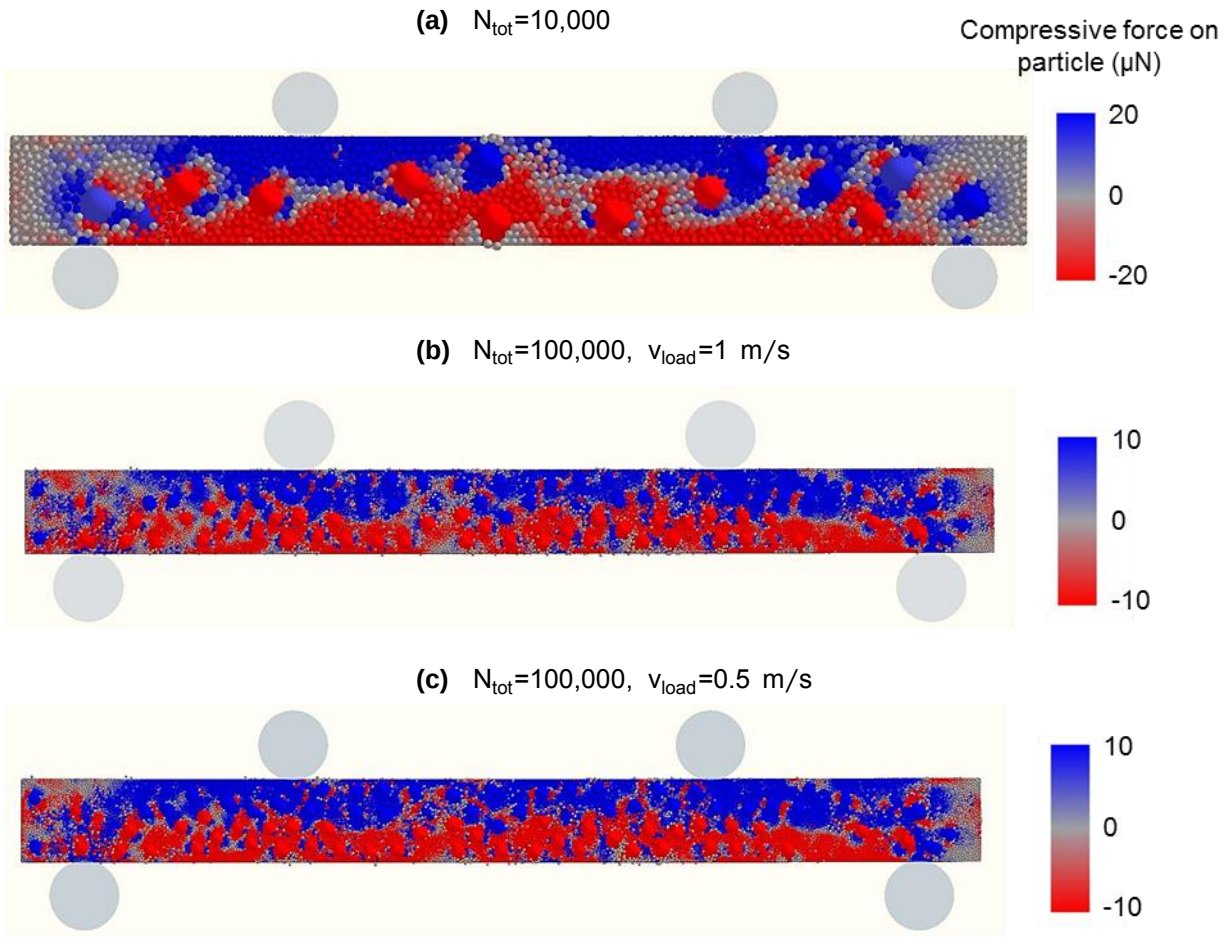

Source: Elaborated by the author.

During the loading, the beams were divided into subsections to study the force network within the beams under applied load (Figure 35). 36 subsections were done for the sample with N_{tot} = 10,000 particles and 45 for the sample with N_{tot} = 100,000 particles. They are divided in three zones along the height, representing the part of the beams which is under compression, the neutral axis and the part under tensile stress. The distribution along the width of the beam was, as expected by symmetry,

rather constant throughout all tests. Therefore, no subdivision was done in this direction.

Figure 35 presents the sum of stresses of all particles inside the subsections, where positive values mean compression and negative values mean tension. The blue color indicates an area where the compression is predominant and the red color where the tension is predominant. The green color indicates areas where there is no predominance of tension or compression. It is possible to see the regions of constant stress formed (almost symmetrically for compression and tension) between the cylinders. The neutral axis in the middle is clearly visible, with some areas of stress because of the steel particle sizes.

Figure 35 - Distribution of total compressive force per subsections on particles during the bending tests on samples with 70 vol.% steel.

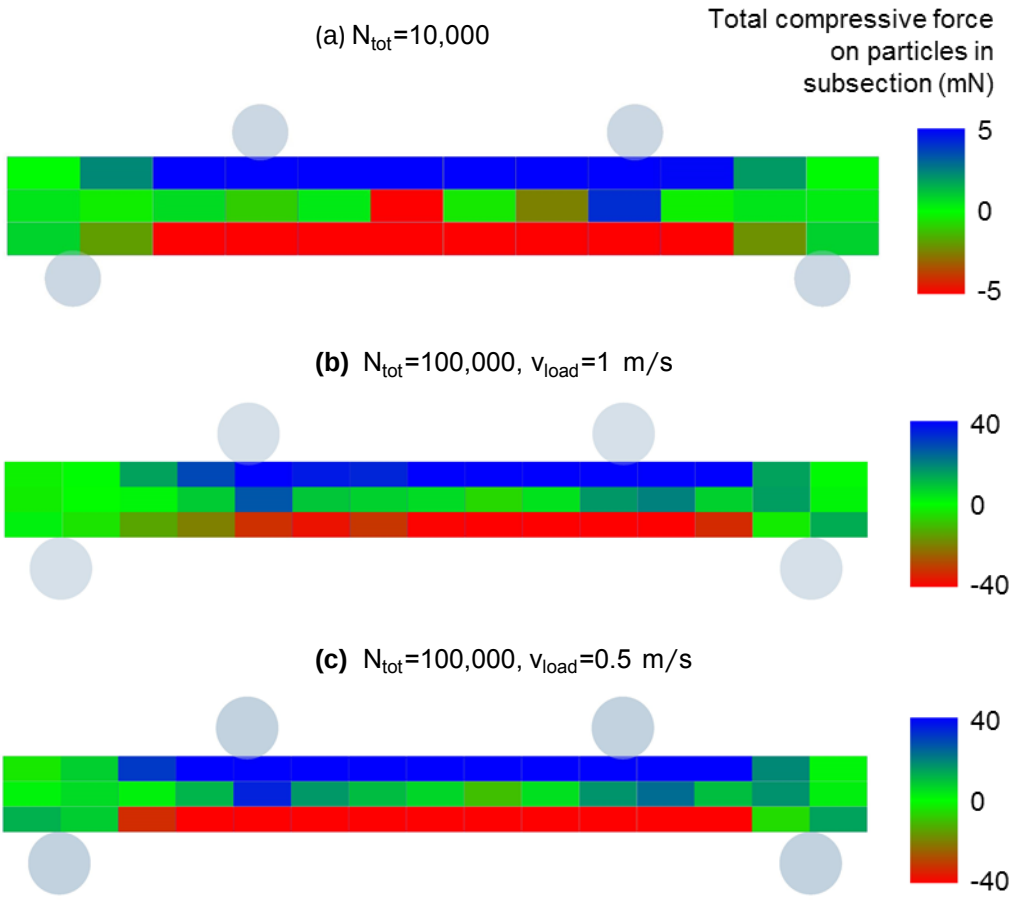

Source: Elaborated by the author.

Figure 36 presents the loading on the sample with 50 vol.% steel. The test was carried out at 1 m/s. The mechanical behavior is similar to the samples with

70 vol.% steel. As expected, the upper part is in compression and the lower part in tension. In Figure 36a, a straight neutral axis with the alumina particles is visible. Since the average coordination number of alumina is higher (CN ~ 5.6), they create a bigger interconnected structure which is clearly divided in the zones of stresses.The same effect in some alumina particles in contact with steel is visible. In the upper part of the beam, where compression is expected, there are particles in tension. In the lower part of the beam, where tension is expected, there are particles in compression. As commented before, a detailed discussion will be done later.

The beam was divided in 45 subsections, with three zones along the height. Figure 36b presents the sum of stresses of all particles inside the subsections, with the compression and tension areas indicated by colors. The regions of compression and tesion are formed simmetrically between the upper loads. It is possible to see also how the stress is reduced towards the lower supports.

Figure 36 - Samples with 50 vol.% steel during the bending tests wtih v_{load}= 1 m/s: (a) compressive force on particles and (b) distribution of total compressive force per subsections on particles.

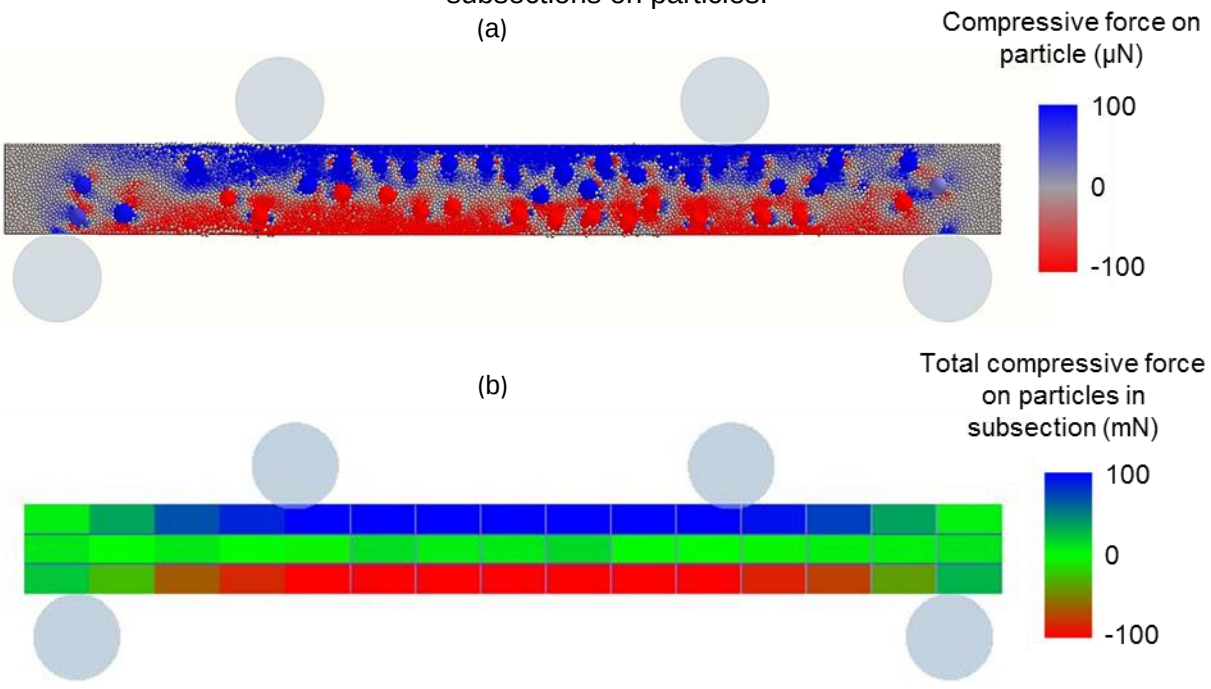

Source: Elaborated by the author.

In Figure 37 the loading stresses are presented for the sample with 30 vol.% steel. The test was carried out at 1 m/s. The steel particles are in lower number and are not clearly visible. The matrix structure of alumina is clearly on bending: the

upper part in compression, the lower part in tension and a straight neutral axis in the middle. It is still possible to find alumina particles in the lower part that are in compression. They are in contact with a steel particle.

The beam was divided in 45 subsections, with three zones along the height. Figure 37b presents the sum of stresses of all particles inside the subsections, with the compression and tension areas indicated by colors. The regions of compression and tension are formed simmetrically between the upper loads. It is also possible to see how the stress is reduced towards the lower supports.

Figure 37 - Samples with 30 vol.% steel during the bending tests with v_{load}=1 m/s: (a) compressive force on particles and (b) distribution of total compressive force per subsections on particles.

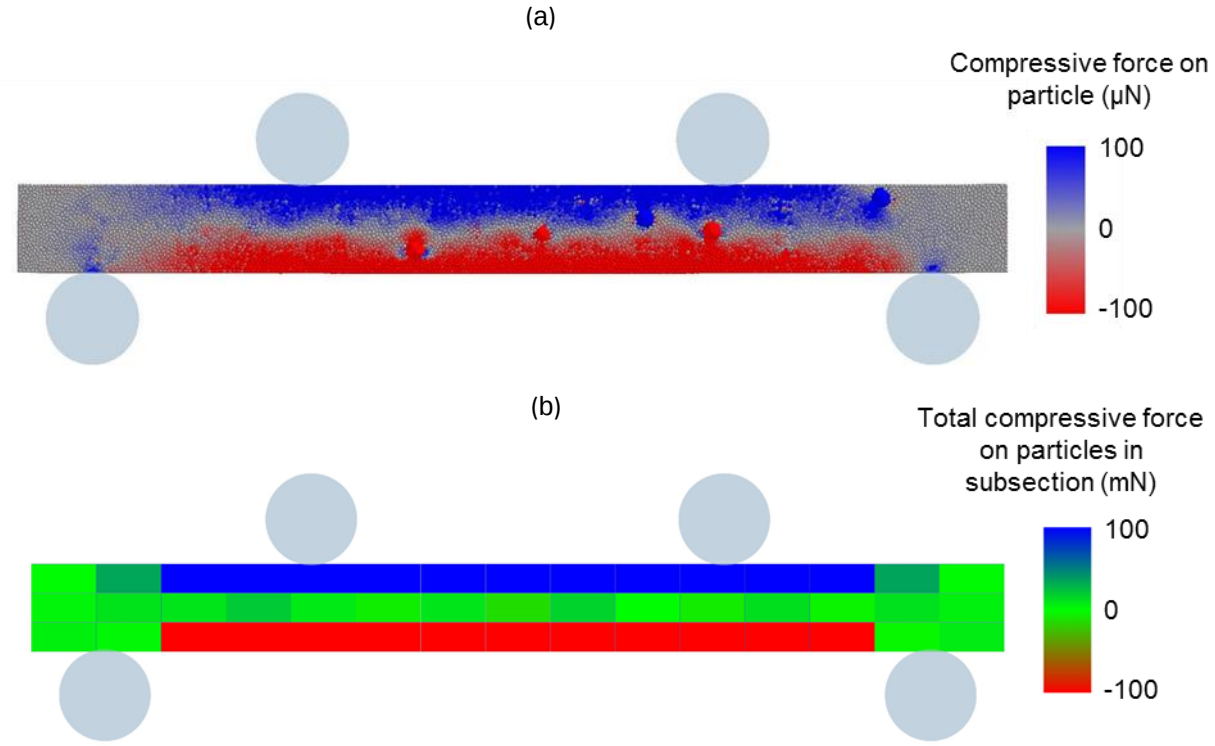

Source: Elaborated by the author.

In Figures 35, 36 and 37, showing the bending of the beams with 70, 50 and 30 vol.% steel, the two length edges do not present regions of stresses. Figure 37 shows clearly that the particles in these regions are not under stresses. This is because the bending moment acting on the beam is null on the edges. There is also a decreasing on stresses between the upper and lower cylinders. This is possible to see within the subsections. The colors change from blue (or red) to green as the

distance become closer to the lower cylinders. This means a decreasing on the bending moment. Figure 38 presents a diagram of the bending moment in a beam under this kind of load. In the middle of the beam, a region of constant bending moment is visible. Between the loading force and the lower supports there is the linear decrease of bending moment. In the edges, the bending moment is null. Therefore, the stresses on this part of the beam are also null.

Figure 38 - Bending moment diagram for a beam under a pair of loads.

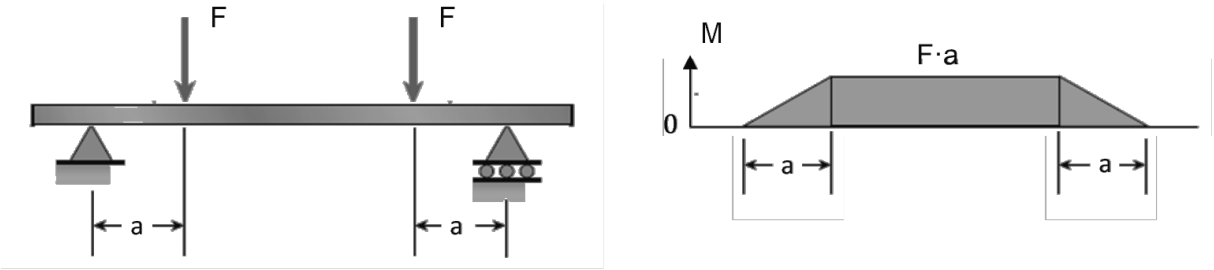

Source: Gere (2004).

4.2.2. FORCE-DISPLACEMENT CURVES

4.2.2.1. Samples with 70 vol.% steel

After the loading, the total forces acting on upper loads is plotted as a fuction of upper loads displacement. Figure 39 presents the curve force-displacement for the beam with N_{tot} = 10,000 particles. For small displacements, a settling of the beam occurs and afterwards the force increases almost linearly. The settling effect happens because the firsts contacts of the upper load with the beam. The elastic modulus of the material was then calculated using equation 4, with the value of the slope $\Delta F^{tot}/\Delta z$ on the linear part of the force-displacement curve (Figure 39a). The resulting value for the elastic modulus was 9.28 GPa.

Figure 39b presents the force-displacement curve for a test with loading and unloading. In the first moments of unloading, there is a small decreasing on the force curve. Afterwards the curve normalizes and behaves similar as the loading curve.

Hysteresis occurs during the first moments and the same behavior is found in real bending tests with this material. The hysteresis means that some lost of energy during the unloading occurs. In the simulation this happens probably because the brekage of bonds.

Figure 39 - Force-displacement curves for bending tests in sample with 70 vol.% steel and N_{tot} = 10,000: (a) loading and (b) loading and unloading.

(a)

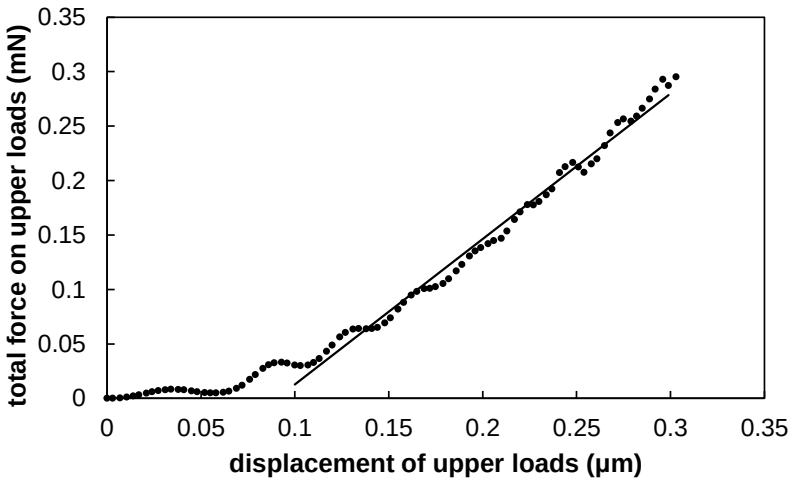

(b)

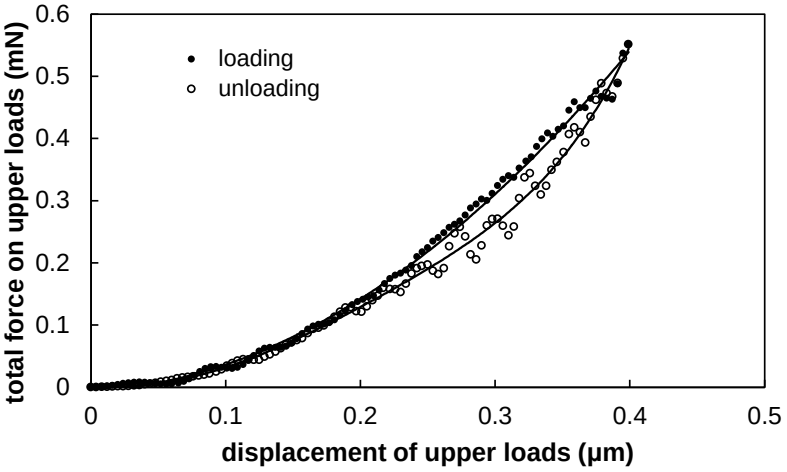

Source: Elaborated by the author.

The force-displacement curve was plotted for the sample with N_{tot} = 100,000 particles, as presented in Figure 40. The curves present a different behavior from the expected. A linear increase was expected as in the test with N_{tot} = 10,000 particles. However, it is possible to see at some moments a big decrease on the force-displacement curve. In Figure 40b, where the loading speed is lower, the decrease occurs four times, since the total displacement of the upper loads is bigger. The cause for this behavior will be explained later.

The obtained curves were used to calculate the elastic modulus of the material. For the test with 1 m/s of loading speed, the slope value of the linear part presented in Figure 40a was used. A value of 132.5 GPa for the elastic modulus was found, which is very similar to the experimental results. In the test at 0.5 m/s of loading speed, three parts of the curve show a linear behavior with almost the same slope. The value for the elastic modulus calculated was 64 GPa.The loading speeds had a big influence on the elastic modulus of the material. Decreasing the velocity by 50%, the simulated elastic modulus is reduced from 132 GPa to 64 GPa. This happen probably because in the test at lower speed the overlap between the upper loads and particles is not big as in the test at at higher speed. The effect of the overlap will be explained later.

Figure 40 - Curves of total force on upper loads and percentage of broken bonds as function of the upper loads displacement for bending tests in sample with 70 vol.% steel and N_{tot} = 100,000: (a) v_{load} = 1 m/s and (b) v_{load} = 0.5 m/s.

(a)

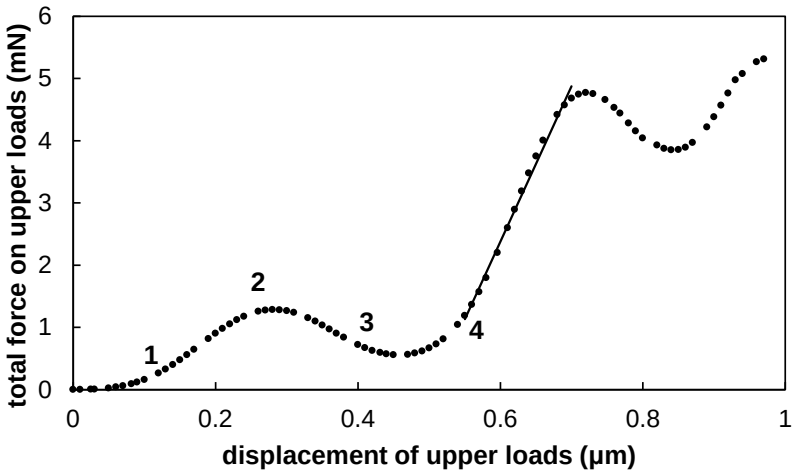

(b)

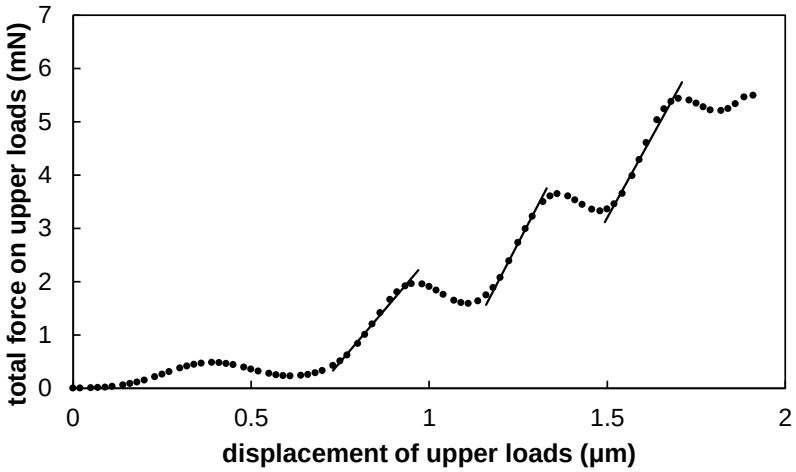

Source: Elaborated by the author.

The drops on the force-displacement curve occur because the rearrangement of the paticles whitin the beam, caused by high forces and broken bonds. During the loading, there is an overlap between the upper loads and the particles. This overlap increases with the increasing displacement, leading to high contact forces. With these high forces, which are transmitted to another particle through the bonds, the particles move downwards and the beam rearranges. The movement of contacting particles with the upper loads can be seen in Figure 41. The 4 moments shown in Figure 40a are represented. The red color is the surface of the upper load, the yellow circles are the alumina particles and the dash line is the initial position of the surface. It is possible to see that all the particles move downwards. With this movement the overlap of particles and upper loads decreases and the force decreases. This causes the drops on the force-displacement curve. After the rearrangement of the beam the force starts to increase again.

Figure 41 - Particles in contact with upper load at the 4 moments shown in Figure 40a. The red color is the upper load surface, the yellow circles are the alumina particles and the dash line is the inital surface position.

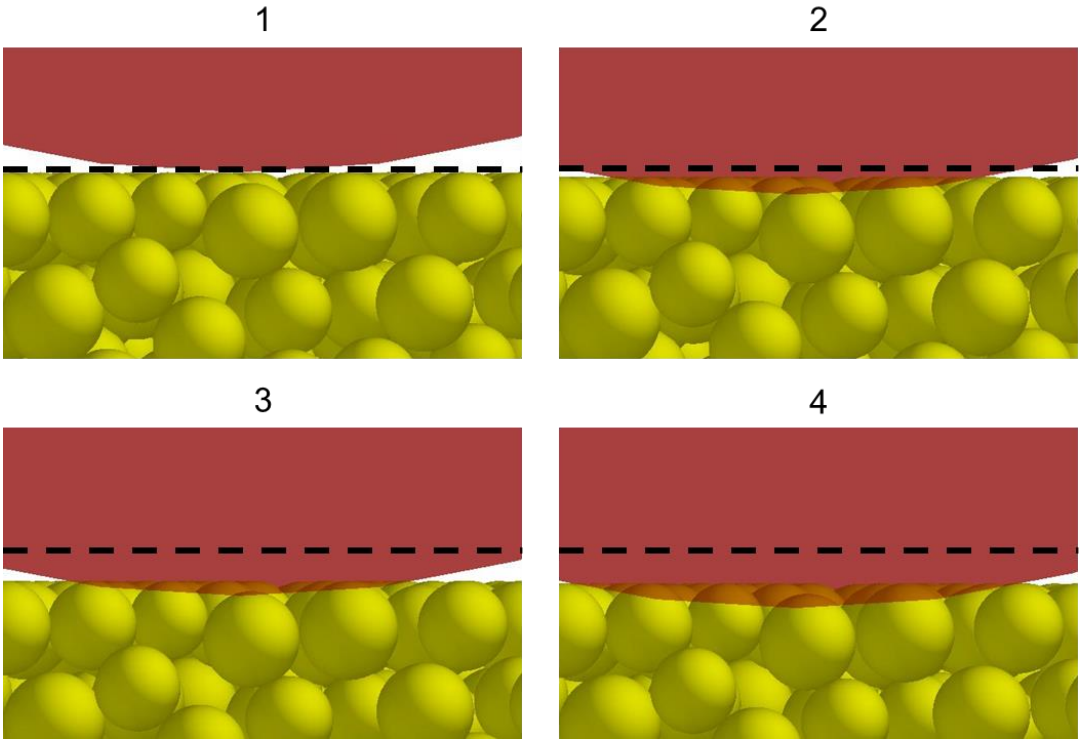

Source: Elaborated by the author.

Since the particles are bonded and form a big structure within the beam, the downward movement of the particles is transmitted to the entire beam. Figure 42

presents this movement during the 4 moments shown in Figure 40a. The first particles to move downwards are in the middle of the beam (moment 2). When they move, the contacting particles also move because they are bonded. This effect is propagated in the x direction to the lenght edges (moment 2-3). After the movement, the particles rearrange and the velocity decreases. The particles in one edge stop moving (moment 3). The stopping effect is propagated until all particles stop (moment 3-4 and 4).

Figure 42 - Velocitiy of particles on sample with 70 vol% steel and v_{load} = 1 m/s, during the 4 moments shown in Figure 40a. The movement starts on the middle of the beam and propagate in the x direction in both ways. After the rearrangement, the particles stop moving.

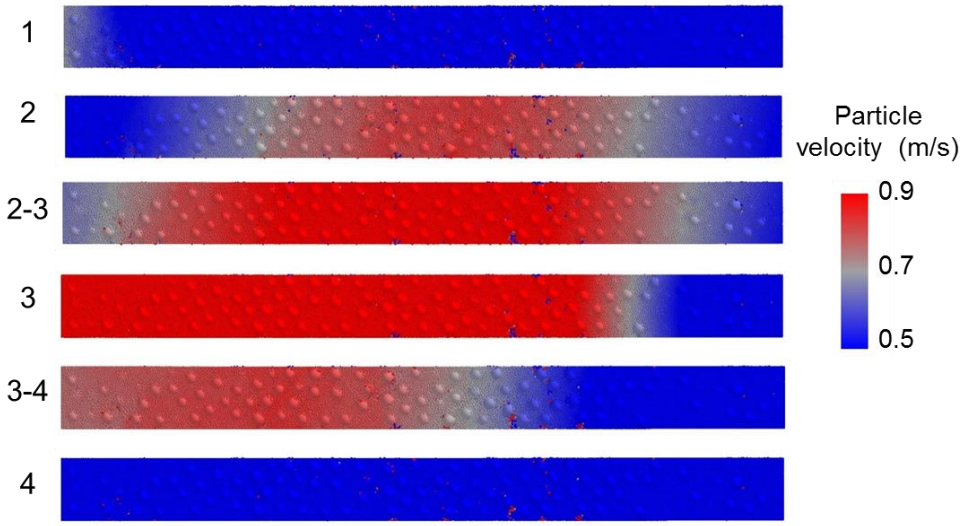

Source: Elaborated by the author.

This propagation of velocities of particles can be proved also with a force-displacement curve on upper and lower cylinders. The curves should be practically similar. However, when the movement of particles starts from the middle of the beam and propagate for the length edges like a wave, the curve for the lower cylinders should be shifted. This is vsible in Figure 43. With the particles downward movement there is the drop of forces on upper loads, since the overlap with particles decreases. When they move downwards there is the increase of the overlap between particles and lower cylinders. Therefore, the force on lower cylinders increases.

Figure 43 - Force-displacement curves for upper and lower cylinders for the bending tests on sample with 70 vol.% steel, N_{tot} = 100,000 and v_{load}= 1 m/s.

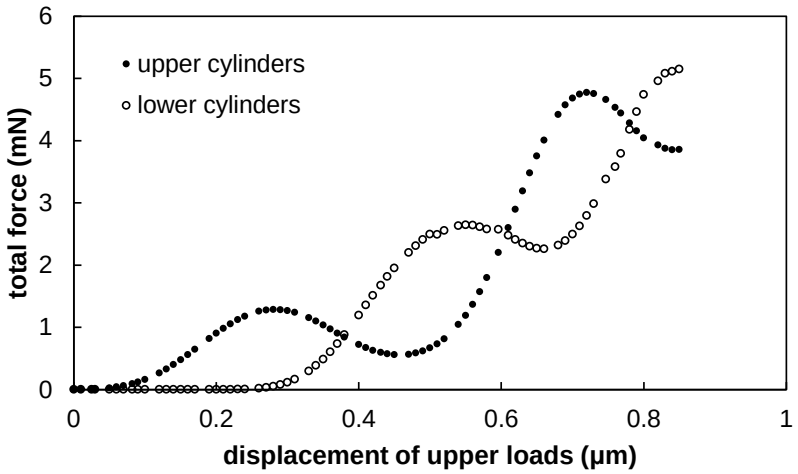

Source: Elaborated by the author.

During this movement of particles, some bonds between alumina particles break. In Figure 44 the percentage of broken bonds is plotted as a function of the displacement. The force-displacement curve is also plotted. The bonds start breaking with the first loading, i.e., the first rising on the force-displacement curve. The number of broken bonds increases highly in the first moments, and afterwards an almost linear increase is found.

Figure 44 - Curves of total force on upper loads and percentage of broken bonds as function of the upper loads displacement for bending tests in sample with 70 vol.% steel, N_{tot} = 100,000 and v_{load}= 1 m/s.

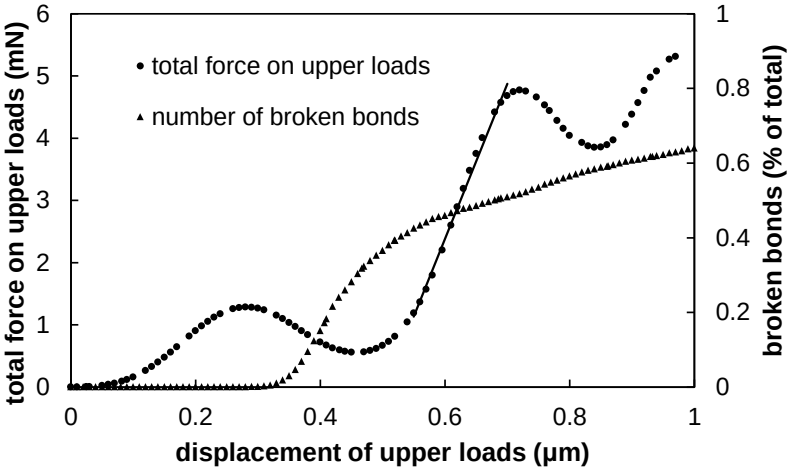

Source: Elaborated by the author.

This has an effect in the beam structure, since the bonds break mostly on the middle part. In Figure 45a, the broken bonds are represented as small black lines. In

Figure 45b, the particles with angular velocity higher then $1 \cdot 10^6$ rad/s are presented. This is a very high value for the angular velocity. The particles are located exactly where the number of broken bonds is higher. The bond breakage results in a high angular velocty. Also, in Figure 45a, it is possible to see the high overlap of the cylinders with the beam, which creates high forces.

After the downward movement of particles, the force increases again. Since the structure presents less bond, a new particle rearragement happens. The movement of particles occur, which causes the second drop on the force-displacement curve.

Figure 45 - (a) positions of broken bonds and (b) position of particles with angular velocity higher than $1 \cdot 10^6$ rad/s in the beam with 70 vol.% steel. The gray circles are the upper and lower cylinders, the black small lines are the broken bonds and the gray dots (b) the centre of particles.

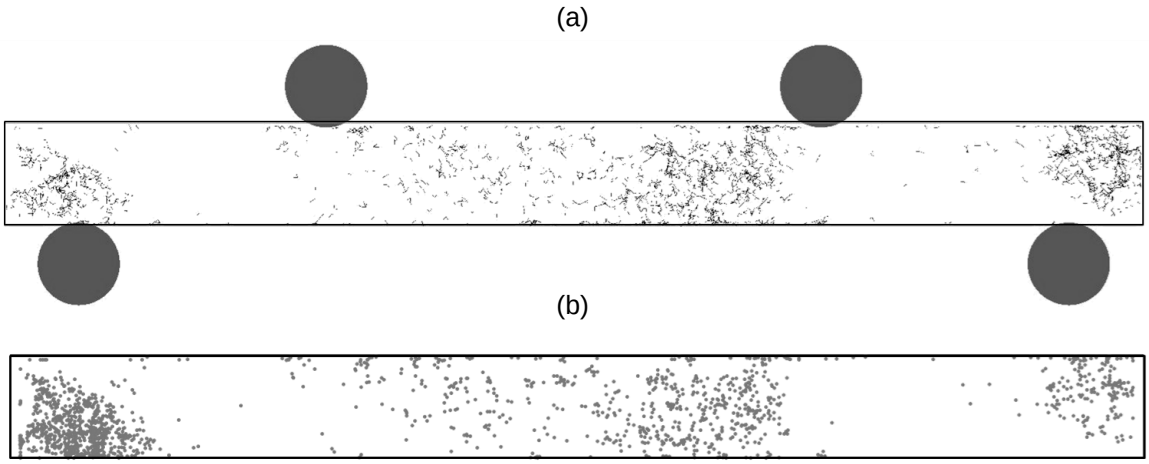

Source: Elaborated by the author.

4.2.2.2. Sample with 50 vol.% steel

The force-displacement curve for the beam with 50 vol.% steel is shown in Figure 46. The percentage of broken bonds is also plotted. The result for the elastic modulus obtained from the force-displacement curve was in the same range as experimental results. By using the slope of the linear part of the curve for the calculation, a elastic modulus of 151 GPa was found.

In Figure 46 a similar decrease is visible on the force-displacement curve as in the test with 70 vol.% steel. Each drop on the force means a movement and

rearrangement of particles downwards. Also, the upper loads creates the overlap with particles as shown in Figure 41, and the velocity of particles is propagated through the beam structure similarly as shown in Figure 42.

Figure 46 - Curves of total force on upper loads and percentage of broken bonds as function of the upper loads displacement for bending tests in sample with 50 vol.% steel, N_{tot} = 100,000 and v_{load}= 1 m/s.

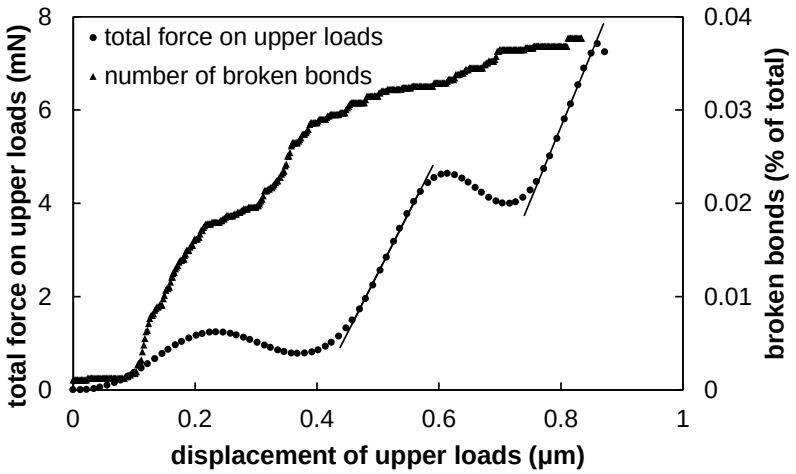

Source: Elaborated by the author.

The number of broken bonds is much lower than in the beam with 70 vol.% steel. This is because the structure formed by the interconnected alumina particles is bigger and thus stronger. The positions of broken bonds in the beam with 50 vol.% steel is different from the one with 70 vol.% steel. The broken bonds in the beam with 70 vol.% steel were mostly in the middle. It is possible to see in Figure 47 that the bonds in the beam with 50 vol.% steel are closer to the upper loads and between the upper and lower cylinders. This creates high forces and a rearrangement of particles, but now in the area near the upper load. When the rearrangement happens the force drops as shown in Figure 46.

Figure 47 - Position of broken bonds in sample with 50 vol.% steel. The gray circles are the upper and lower cylinders and the black small lines are the broken bonds.

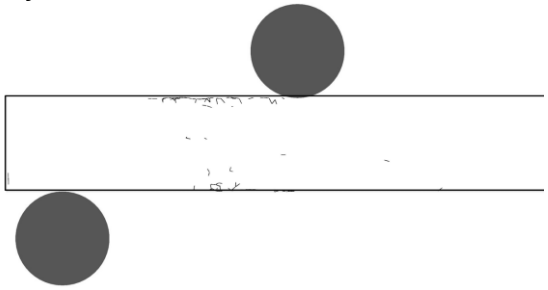

Source: Elaborated by the author.

4.2.2.3. Sample with 30 vol.% steel

The force-displacement curve for the beam with 30 vol.% steel is presented in Figure 48. The percentage of broken bonds is also plotted. The result for the elastic modulus obtained from the force-displacement curve was in agreement with experimental results. By using the slope of the linear part of the curve for the calculation, a elastic modulus of 132 GPa was found.

A similar decrease on the force-displacement curve is visible as in the test with 70 vol.% steel. Each drop on the force means a movement and rearrangement of particles downwards. The upper loads creates the overlap with particles as shown in Figure 41, and the velocity of particles is propagated through the beam structure similarly as shown in Figure 42.

Figure 48 - Curves of total force on upper loads and percentage of broken bonds as function of the upper loads displacement for bending tests in sample with 30 vol.% steel, N_{tot} = 100,000 and v_{load}= 1 m/s.

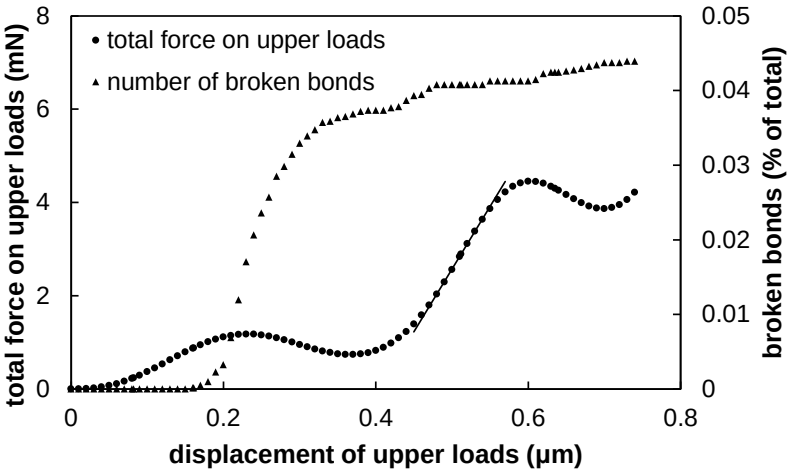

Source: Elaborated by the author.

The number of broken bonds is lower than in the test with 70 vol.% steel and similar to the test with 50 vol.% steel. The alumina in this case is the matrix. A higher number of bond is created and the alumina structure is stronger than in the samples with 70 and 50 vol.% steel. Figure 49 presents the positions of broken bonds within the beam after the loading. They are located mostly in the middle of the beam. A random distribution of broken bonds is found within the length. The rearragement of particles happens since there is a layer of broken bonds in the middle.

Figure 49 - Position of broken bonds in sample with 30 vol.% steel. The gray circles are the upper and lower cylinders and the black small lines are the broken bonds.

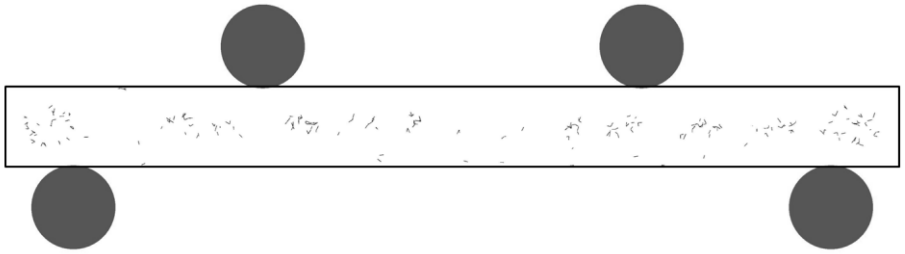

Source: Elaborated by the author.

4.2.3. RESULTS ON ELASTIC MODULUS

The real experiments were carried out on beams with about 40 to 50 mm of length. For the production of beams, the steel 1.2344 powder was mixed with two types of alumina: Almatis CT 3000 SG and Taimei DAR 100 TM. The first is constituted of particles with an average diameter of 0.88 μm, and the second 0.1 μm.

To process of fabrication included the steps of powder mixing, unixial pressing, cold isostatic pressing and sintering, respectively. The mixing was carried in an atrition mill, using a polyvinil alcohol binder to ensure the stability of the green body during compaction. The powder was dryied in a rotatory evaporator. The unixial pressing was carried at pressures varying from 50 to 250 MPa and CIP pressing from 100 to 500 MPa, depending on the composition. The green bodies using Taimei and Almatis present similar relative densities: 0,64 for 30 vol. % steel, 0,7 for 50 vol. % steel and 0,72 for 70 vol. % steel. It is important to note that in the simulations the packing density achieved was realtive similar to the green densities of the real samples.

Sintering was carried using a eigth-step heating process. In Table 10, the average relative densities of samples after sintering with different alumina powders are presented, comparing with the elastic modulus obtained in the bending tests. With Taimei powder a higher relative density is reached. This is because the lower size of particles, which gives the powder a higher sintering reactivity. For Almatis powder, the sintering temperature necessary to reach 98% of relative density is 1540^{o}C. For Taimei the sintering temperature is 1350^{o}C to reach the same relative density.

The difference on relative densities has a big effect on the elastic modulus. For the composition with 70 vol.% steel, the average relative density with Taimei powder is just 4% higher than with Almatis. The elastic modulus is 67% higher with the Taimei powder. For the composition with 30 vol.% steel, the average relative density with Taimei powder is 13% higher than with Almatis. However, the elastic modulus is just 5% higher with the Taimei powder.

Table 10 - Results for elastic modulus in real and virtual experiments.

vol.% steel	Almatis		Taimei		Simulation	
	ρ_r	***E* (GPa)**	ρ_r	***E* (GPa)**	ρ_p	***E* (GPa)**
70	85%	146	89%	244	63.5%	159
50	81%	131	90%	184	66.3%	151
30	77%	132	90%	139	60.5%	132

Source: Elaborated by the author.

Figure 50 presents the results of elastic modulus and densities plotted as function of steel fraction. In the simulation with 70 vol.% steel, the elastic modulus is just 8% higher than the results with Almatis powder. For 50 vol.% steel, a value between the results with Almatis and Taimei is obtained. This is because the packing density of the simulated beam with 50 vol.% steel is higher than with 70 or 30 vol% steel, as can be seen in Table 10. The samples with Taimei powder have a higher relative density than with Almatis. The simulation results approximates in a small amount the Taimei results. For the composition with 30 vol.% a lower packing density is accomplished and the value of elastic modulus obtained is exactly the same as the results with Almatis.

Figure 50 - (a) relative density of real samples and packing density of simulated beams for different compositions and (b) results for elastic modulus plotted as function of steel fraction.

(a)

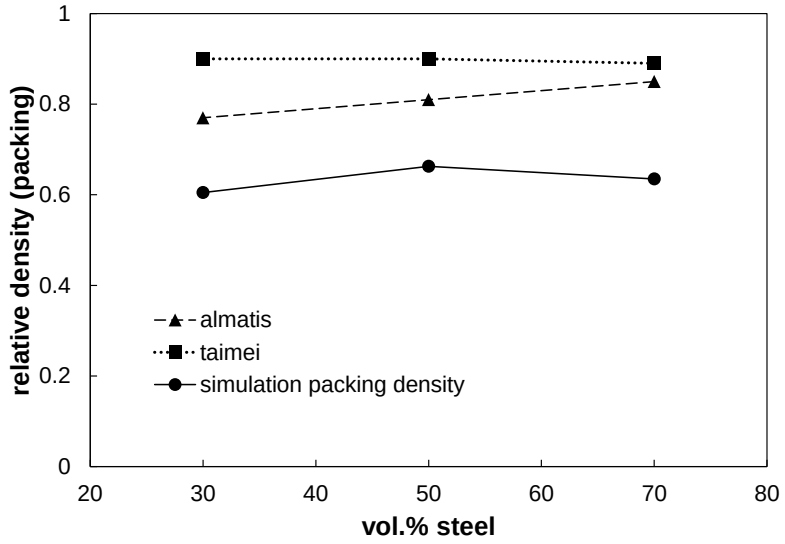

(b)

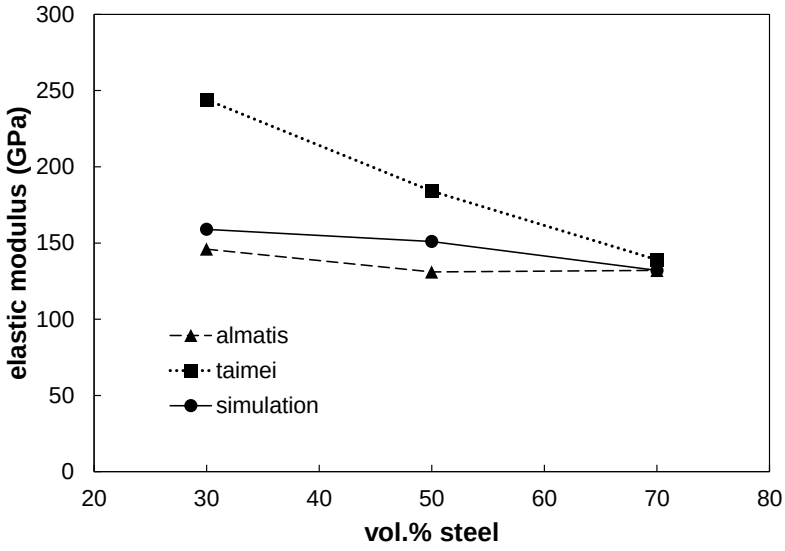

Source: Elaborated by the author.

4.2.4. METAL – CERAMIC CONTACT BEHAVIOR DURING BENDING

As showed in the earlier subsection, a very interesting behavior occurs with some alumina particles in contact with steel during the bending tests. In areas where compression stresses on particles were expected, some particles are in tension, and in areas where tension was expected, some particles were in compression. Figure 51

presents the particles in the different stress zones of the beam with 70 vol.% steel. The blue color indicates compression and the red color indicates tension. In the upper part, where compression is expected, there are alumina particles in tension. These particles are mostly between two or more steel particles. In the lower part, where tension is expected, there are particles in compression. They are also between two or more steel particles. This is also found with the compositions of 50 and 30 vol% steel, but less frequently since the number of steel particles decreases.

The main contact law between alumina and steel particles is the Hertz-Mindlin-Tsuji model, which contains a frictional part. A high friction coefficient was used in steel-alumina interactions. During the bending test, there is particle movement. The alumina particles are subjected to the forces from the bonds between another alumina particles. Those which are located between steel particles are subjected also by high frictional forces. Thus, they can be pulled by the bonds to one direction, and can be subjected to friction forces to another direction because of the movement of steel particles. The particle will be then in tension, which can be seen also in the compression zones of the beam.

In the tension zone, the alumina particles are pulled from both sides by the bonds with oher alumina particles. This leads to tension stress. If bonding was created between steel and alumina, the alumina particles would be pulled also by the bonds between steel. There would be only particles in tension in the lower part of the beam. However, no bonding was created between steel and alumina. Therefore, when an alumina particle is in contact with steel, it is subjected to normal forces from the contact model. With the movement of steel particles during the bending, the overlap between some steel and alumina particles increases. When an alumina particle is located between two steel particles, the overlap can increase from both sides. The normal forces will increase. This leads to compression stress on the particle.

Figure 51 - Compression and tension forces on particles in different zones of the beam.

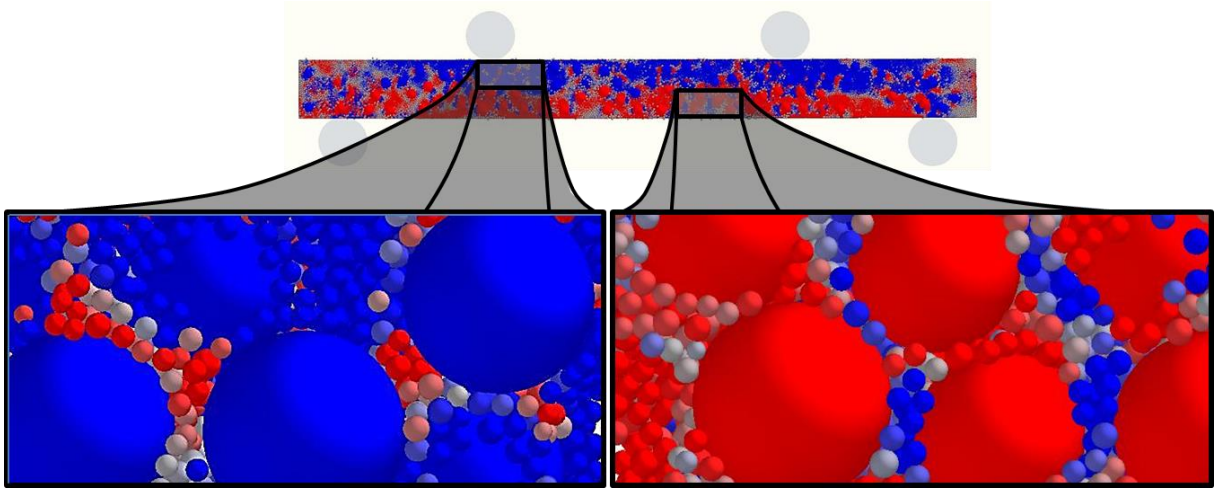

Source: Elaborated by the author.

5. CONCLUSIONS

The discrete element method was used to simulate the mechanical behavior in four-point bending test of a steel and alumina composite. Three compositions were simulated containing 30, 50 and 70 vol.% of steel.

Beams were generated by compression and presented a random distribution within all directions of the beam. Particle size ratio has a significant effect on structure formed with different amounts. Since alumina particles are smaller in diameter, the amount necessary to create a percolated structure is lower than for steel. With 30 vol% of alumina, a interpenetrating structure is formed in the steel matrix. However, with 30 vol.% of steel, the structure is formed by steel inclusions on the alumina matrix.

The approach with the bonding model was tested and validated for the compositions. The generation of tension and compression regions was observed in all cases. The forces and stresses are transmitted between the bonded particles similarly as sintered samples.

The force-displacement curves were obtained from the bending tests. Big decreases in the curve were seen. This occur because the high forces and overlaps on particles in contact with upper loads. This leads to bonds breakage and rearragement of particles within the beam.

The values for elastic modulus obtained were satisfying. A comparison with results from samples produced with two different alumina powders was done. It was seen that the values from simulations were in good agreement. A relashionship was found on the relative densities of real samples and packing density of simulated beams with the elastic modulus. The packing density in the simulation is not related with the density of sintered body. However, it seems to have a influence on the results.

The results on tests at 1 m/s were in agreement with experimental results. However, this changes when a lower velocity for the loading is used. It was seen that decreasing the velocity by 50%, the simulated elastic modulus is reduced in almost 50%. The number of particles also influence on the elastic modulus. In the simulation with N_{tot}= 10,000 particles particles, a value 95% lower than in simulations with N_{tot}= 100,000 particles was obtained. The structure of the generated beam was small to reach good results.

The DEM is a powerful and interesting resource for particulate material researches. Several aspects that influence the mechanical behavior on composites, such as aggregates and interpenetrate structure, particle size distributions, bond breakage and particle movement during bending can be analized. The method with bonds is suitable for simulation of greenbody and injection molds products. A detailed insight on the bonding of particulates composites should be done to validate the bonding model as an effective model for a sintered material.

REFERENCES

AL-QURESHI, H. A. **Materiais Compostos: análises e fabricação**. 1. ed. Joinville: Universidade Federal de Santa Catarina, 2010.

AMERICAN SOCIETY FOR TESTING AND MATERIALS. **C1161-13**: Standard test method for flexural strength of advanced ceramics at ambient temperature. West Conshohocken: ASTM, 2013.

ANTONYUK, S.; HEINRICH, S.; TOMAS, J.; DEEN, N. G.; BUIJTENEN, M. S.; KUIPERS, J. A. M. Energy absorption during compression and impact of dry elastic-plastic spherical granules. **Granular Matter**, v. 12, p. 15–47, jan. 2010.

BARRY, C. C.; GRANT, M. N. **Ceramic Materials**: science and engineering. Nova Iorque: Springer, 2007.

BLACK, J. T; KOHSER, R. A. **Degarmo's Materials And Processes In Manufacturing**. 10. ed. Hoboken: John Wiley & Sons, 2008.

BOUVARD, D. Densification behaviour of mixtures of hard and soft powders under pressure. **Powder Technology**, v. 111, p. 231–239, ago. 2000.

CUNDALL, P. A.; STRACK, O. D. L. A discrete numerical model for granular assemblies. **Géotechnique**, v. 29, p. 47-65, 1979.

DEEN, N. G.; VAN SINT ANNALAND, M.; VAN DER HOEF, M.A.; KUIPERS, J.A.M. Review of discrete particle modeling of fluidized beds. **Chemical Engineering Science**, v. 62, p. 28–44, ago. 2006.

DEM SOLUTIONS. **EDEM® Academic v 2.5 User Guide 1**. DEM Solutions Ltd.

EUROPEAN POWDER METALLURGY ASSOCIATION. **Powder Metallurgy**: the process and its products. Shrewsbury: EPMA, 2008.

GERE, J. M. **Mechanics of Materials**. 6. ed. Belmont: Thomson Learning, 2004.

GOGOTSI, G. A. Fracture toughness of ceramics and ceramic composites. **Ceramics International**, v. 29, p. 777–784, 2003.

HENRICH, B.; WONISCH, A.; KRAFT, T.; MOSELER, M.; RIEDEL, H. Simulations of the influence of rearrangement during sintering. **Acta Materialia**, v. 55, p. 753–762, nov. 2006.

HERTZ, H. Über die Berührung fester elastischer Körper. **Journal für die reine und angewandte Mathematik**, v. 92, p. 156–171, 1882.

JI, S.; LI, Z.; LI, C. Discrete element modeling of ice loads on ship hulls in broken ice fields. Acta Oceanol. Sin. 32, p. 50–58, maio 2013.

LAU, M. **Discrete element modeling of ship maneuvering in ice**. Canada: National Research Council, 2013.

MARTIN, C. L.; BOUVARD, D. Isostatic compaction of bimodal powder mixtures and composites. **International Journal of Mechanical Sciences**, v. 46, p. 907–927, maio 2004.

MINDLIN, R.D.; DERESIEWICZ, H. Elastic spheres in contact under varying oblique forces. **Journal of Applied Mechanics**, p. 327–344, 1953.

MIYAGI, Y. Application of Ceramics to Marine Diesel Engines. **Mechanical Engineering – Scientific Journal**, v. 28, p. 69-77, jun 1993.

NOHUT, S. Prediction of crack-tip toughness of alumina for given residual stresses with parallel-bonded-particle model. **Computational Materials Science**, v. 50, p. 1509–1519, jan. 2011.

OLMOS, L.; MARTIN, C. L.; BOUVARD, D. Sintering of mixtures of powders: Experiments and modelling. **Powder Technology**, v. 190, p. 134–140, maio 2008.

POTYONDY, D. O.; CUNDALL, P. A. A bonded-particle model for rock. **International Journal of Rock Mechanics and Mining Sciences**, v. 41, p. 1329–1364, out. 2004.

RICHERSON, D. W. **Modern ceramic engineering**: properties, processing, and use in design. 3. ed. Nova Iorque: Taylor & Francis, 2006.

SALVAGNI, P. **Investigation of stability of large pores in alumina films during the sintering by discrete element method simulation**. 2013. 77 f. TCC (Graduação) - Curso de Engenharia Mecânica, UFSC, Florianopolis, 2013.

SCHILDE, C.; BURMEISTER, C. F.; KWADE, A. Measurement and simulation of micromechanical properties of nanostructured aggregates via nanoindentation and DEM-simulation. **Powder Technology**, v. 259, p. 1–13, mar. 2014.

SCHWARTZ, M. M. **Composite materials handbook**. 2. ed. Nova Iorque: McGraw-Hill, 1992.

SHARMA, A. K.; GUPTA, D. On microstructure and flexural strength of metal–ceramic composite cladding developed through microwave heating. **Applied Surface Science**, v. 258, p. 5583–5592, mar. 2012.

SKRINJAR, O.; LARSSON, P. On discrete element modelling of compaction of powders with size ratio. **Computational Materials Science**, v. 31, p. 131–146, fev. 2004.

SPANDONIDIS, C. C.; SPYROU, K. J. Micro-scale modeling of excited granular ship cargos: a numerical approach. **Ocean Engineering** , v 74, p. 22–36, 2013.

TSUJI, Y.; TANAKA, T.; ISHIDA, T. Lagrangian numerical simulation of plug flow of cohesionless particles in a horizontal pipe. **Powder Technology**, v. 71, p. 239–250, 1992.

WOLFF, M.F.H.; SALIKOV, V.; ANTONYUK, S.; HEINRICH, S.; SCHNEIDER, G. A. Three-dimensional discrete element modeling of micromechanical bending tests of ceramic–polymer composite materials. **Powder Technology**, v. 248, p. 77–83, jul. 2013.

ZHU, H. P.; ZHOU, Z. Y.; YANG, R. Y.; YU, A. B. Discrete particle simulation of particulate systems: A review of major applications and findings. **Chemical Engineering Science**, v. 63, p. 5728–5770, ago. 2008.